19 (2026) 100633

Contents lists available at ScienceDirect

Carbon Capture Science & Technology

journal homepage: www.elsevier.com/locate/ccst

Full Length Article

Investigation on the cyclic CO_2 capture behaviour and degradation mechanism of molten salt promoted MgO derived from commercial hydromagnesite

Sumit Chakraborty [a,b,*], Paul Fennell [a]

[a] Department of Chemical Engineering, Imperial College London, London, SW7 2AZ, UK
[b] Chirasree Centre for Sustainable Infrastructure Development (CCSID), Indian Institute of Engineering Science Technology, Shibpur, Botanical Garden, Howrah, West Bengal 711103, India

ARTICLE INFO

Keywords:
CO_2 capture
MgO Sorbent
Molten salts
Layer double hydroxide (LDH)
Alkali- metal nitrates

ABSTRACT

This study examines the cyclic CO_2 capture performance and degradation mechanism of molten salt-promoted MgO, a low-cost and scalable precursor, derived from commercially available hydromagnesite. The material was modified using different nitrate-based molten salt compositions to enhance CO_2 uptake. Among the formulations, single- and double-salt-promoted MgO exhibited the highest initial capture capacities; however, performance declined with repeated cycling. Notably, the single-salt system demonstrated comparatively better stability over 10–22 cycles than others. The observed reduction in CO_2 capture capacity is attributed to the gradual loss and transformation of nitrate species, which reduces the effective molten phase and pore blockage. Thermodynamic analysis supports the conversion of active nitrate phases into less effective forms during cycling, while X-ray diffraction and ICP-MS confirm a decrease in nitrate content despite minimal change in overall sodium levels. These findings highlight the critical role of molten salt stability in sustaining CO_2 capture performance and provide insight into the design of more durable MgO-based sorbents.

1. Introduction

The global climate emergency calls for a drastic reduction in CO_2 emissions across all sectors (Climate change and human behaviour, 2022; Meinshausen et al., 2009) and emphasizes the need for carbon-free alternatives in energy systems to achieve the goal of net-zero by 2050. Due to the limited availability of alternative energy sources, fossil fuels remain a dominant energy source, contributing the largest share of greenhouse gas emissions and significantly impacting the climate. This has made the development and implementation of advanced CO_2 capture and storage technologies essential (Qiao et al., 2017). Considerable efforts are being made to develop new technologies, processes, and materials for CO_2 capture, utilization, and storage (CCUS) that align with the requirements of energy systems (Wenxing et al., 2025; Wang et al., 2014b; Ruminski et al., 2011).

Three principal approaches; pre-combustion capture, post-combustion capture, and oxy-fuel combustion capture are commonly suggested to decarbonise processes (Gao et al., 2017; Ruhaimi et al., 2021; Wang et al., 2011; Zheng et al., 2016). Although aqueous-based solvents (Gao et al., 2020; Dong et al., 2022; Rochelle, 2009; Stolaroff et al., 2008; D'Alessandro et al., 2010, Olajire, 2013) are widely used for CO_2 capture, they are frequently applied in post-combustion systems due to their operation at relatively low temperatures (Qiao et al., 2017). Pre-combustion CO_2 capture is exemplified by integrated gasification combined cycle (IGCC) systems and related processes such as sorption-enhanced water–gas shift (SEWGS) and sorption-enhanced biomass reforming (SEBR). These processes (Abbasi et al, 2014; Norouzpour et al., 2025; Qin et al., 2017) utilise solid adsorbents over a broad temperature range (200–700°C) (Qiao et al., 2017; Gao et al., 2017). Among solid adsorbents, including zeolites (Bhatta et al., 2015), metal–organic frameworks (MOFs) (Azmi and Aziz, 2019; Modak and Jana, 2019, Welton et al., 2025), silica (Wang et al., 2024;), carbon (Zeng et al., 2018; Adegoke and Tseki, 2025), and microwave assisted CO_2 absorption (Shi et al., 2026), metal oxides offer several advantages (Qiao et al., 2017; Gao et al., 2017; Wang et al., 2025a). These include their abundance, low cost, low toxicity, broad applicability across temperature and pressure conditions, high working capacity, and ease of disposal without significant environmental hazards

* Corresponding author.
E-mail address: sumit.chakraborty@imperial.ac.uk (S. Chakraborty).

https://doi.org/10.1016/j.ccst.2026.100633
Received 23 March 2026; Received in revised form 19 May 2026; Accepted 19 May 2026
Available online 19 May 2026
2772-6568/© 2026 The Authors. Published by Elsevier Ltd on behalf of Institution of Chemical Engineers (IChemE). This is an open access article under the CC BY license (http://creativecommons.org/licenses/by/4.0/).

(Qiao et al., 2017; Wenxing et al., 2025; Ruhaimi et al., 2021; Vu et al., 2014; Wang et al., 2014a). Among the various alkaline earth metal oxides (CaO, MgO, BaO, Fe_2O_3), MgO is considered one of the more promising sorbents for CO_2 capture in SEWGS and SEBR processes, particularly within the temperature range of 200–400°C, owing to its high theoretical CO_2 uptake (24.8 mol·kg^{-1}) (Qiao et al., 2017; Gao et al., 2017). However, it has been reported that, in practice, the CO_2 capture capacity of MgO synthesised from layered double hydroxides is limited due to slow reaction kinetics and poor thermal stability (Bhatta et al., 2015). Consequently, significant efforts have been directed toward enhancing its adsorption performance through approaches such as precipitation from mixed oxides (Li et al., 2013), dispersion on porous supports (Li et al., 2014), and modification with molten salts (Harada and Hatton, 2015).

In recent years, the synthesis of molten salt-modified MgO and its application in SEWGS have attracted increasing attention for CO_2 capture (Qiao et al., 2017; Gao et al., 2017; Ruhaimi et al., 2021; Prashar et al., 2016; Cai et al., 2022; Gao et al., 2022). Fig. S1 illustrates publication trends over the past decade—based on search terms including "metal oxide for CO_2 capture," "MgO for CO_2 capture," "molten salt-promoted MgO for CO_2 capture," and "nitrate-promoted MgO for CO_2 capture"—highlighting the growing interest in molten salt-modified metal oxides for CO_2 capture on the Web of Science platform. Significant research efforts were devoted to produce molten salt-promoted absorbents as they demonstrated excellent CO_2 capture performance, regeneration capability, and considerable thermal stability (Qiao et al., 2017; Gao et al., 2017; Ruhaimi et al., 2021; Prashar et al., 2016; Gao et al., 2022; Harada et al, 2015; Jin et al., 2017; Zhang et al., 2013; Chen et al., 2021; Gui et al., 2024). Research interest in molten salt-promoted MgO was accelerated after a US patent was granted for sorbents with a wide range of CO_2 capture capacity 1.1-12.9 mol.kg^{-1} depending on the synthesis condition and capture parameters (Mayorga et al., 2001).

Various mechanisms have been reported to promote the CO_2 capture capacity of molten salt–modified MgO (Qiao et al., 2017; Gao et al., 2017; Gao et al., 2022; Landuyt et al., 2022; Bork et al., 2022). It has been suggested that the molten salt provides liquid channels for rapid CO_2 diffusion (Cai et al., 2022). The enhanced CO_2 capture capacity of $NaNO_3$-promoted MgO has been attributed to the substitution of nitrate groups into the $MgCO_3$ lattice, resulting in increased lattice defects after partial desorption of CO_2 (Prashar et al., 2016). Other studies have proposed that the molten salt acts as a medium for dissolving both the sorbent and CO_2, thereby reducing the relative stability of $MgCO_3$ during desorption and enhancing adsorption kinetics (Shen et al., 2023). Equations 1–3 illustrate the chemical reactions involving $NaNO_3$--promoted MgO during the adsorption and desorption processes (Jo et al., 2017).

Adsorption:

$$MgO + NaNO_3 + CO_2 \xrightarrow{270\ ^\circ C} MgCO_3 + NaNO_3 \quad (1)$$

Desorption:

$$MgCO_3 + NaNO_3 \xrightarrow{400\ ^\circ C} MgO + NaNO_3 + CO_2 \quad (2)$$

Decomposition:

$$2NaNO_3 \xrightarrow{550\ ^\circ C} 2NaNO_2 + O_2 \quad (3)$$

Although $NaNO_3$ typically decomposes at or above 550°C, repeated CO_2 sorption–desorption cycles may induce its degradation even below this temperature (Bond and Jacobs 1966). It is widely accepted that molten salts are dispersed over the sorbent surface, rendering it partially wetted during both sorption and desorption. This facilitates the partial dissolution of solid MgO in the molten salt, forming solvated ion pairs [$Mg^{2+}\cdots O^{2-}$] (Gao et al., 2017). Ultimately, the sorbent system can overcome strong lattice constraints (Zhang et al., 2014), thereby enhancing CO_2 capture kinetics through adsorption on the MgO surface and the formation of a gas–liquid–solid triple-phase boundary (TPB) (Qiao et al., 2017; Gao et al., 2017). In this process, gaseous CO_2 molecules adsorb onto the bare MgO surface to form the TPB and react with the solvated ion pairs, followed by the precipitation of $MgCO_3$ away from the initial dissolution site, thereby sustaining continued CO_2 uptake (Qiao et al., 2017; Gao et al., 2017; Gao et al., 2022).

Qiao et al. (2017) reported cyclical CO_2 capture for triple-salt-modified MgO and observed a pronounced decline in capacity (from 16.8 to 3.2 mol/kg after 15 cycles); the underlying degradation mechanisms were not systematically elucidated. Zhang et al. (2014) demonstrated that molten salts can act as phase-transfer catalysts, achieving CO_2 uptake of up to 15 mol/ kg, while Pozzo et al. (2019) attributed cyclic performance decay primarily to partial sintering of the sorbent.

The literature review reveals that previous studies have largely established the fundamental mechanisms responsible for the high initial CO_2 capture performance of molten salt–promoted MgO sorbents, particularly following single or limited sorption–desorption tests. Moreover, the influence of molten salt chemistry, desorption temperature, and salt phase evolution on regeneration efficiency and long-term cyclic stability has received little focused attention. In particular, degradation and transformation pathways of different molten salt systems during repeated CO_2 capture–regeneration cycles remain poorly understood.

This study presents a systematic investigation into the role of molten salt chemistry on MgO-based CO_2 capture performance. The impact of single salt (SS: 10 mol% $NaNO_3$), double salts (DS: 7 mol% $NaNO_3$ + 4 mol% $NaNO_2$), and triple salt (TS: 2 mol% $LiNO_3$ + 7.6 mol% $NaNO_3$ + 0.4 mol% Na_2CO_3) modified MgO sorbents has been comparatively evaluated under multiple adsorption (300 and 310°C) and desorption (380, 400, and 450°C) conditions, together with extended cyclic CO_2 capture testing. In this study, the degradation and phase transformation mechanisms of these molten salt systems during cyclical operation are elucidated through thermodynamic modelling using FactSage 8.0, and are rigorously validated by complementary ICP-MS, XRD, and FTIR analyses. This integrated experimental-thermodynamic approach provides new mechanistic insights into salt stability and sorbent performance, offering a robust framework for the rational design of durable MgO-based CO_2 capture materials.

2. Experimental

2.1. Materials

Commercial hydro-magnesite (>90% purity, chemical formula $4MgCO_3{\cdot}Mg(OH)_2{\cdot}4H_2O$; <1% quartz, balance: moisture) supplied by Inoxia Ltd, UK, was used as the primary MgO source material. Additionally, 99% pure $LiNO_3$, $NaNO_3$, $NaNO_2$, $Na_2CO_3{\cdot}10H_2O$, and methanol were purchased from Merck Life Science UK Limited to synthesize molten salt promoted MgO.

2.2. Method

2.2.1. Sample preparation

Single (SS), double (DS), and triple salt (TS) promoted MgO were synthesized. The doses of the molten salts were selected from the previous studies by Jin et al., (2017) and Zhao et. al., (2018) as they found high capture capacity with their selected doping methodologies. The primary objective of the present work is to systematically evaluate the cyclical CO_2 sorption behaviour of representative molten salt–modified MgO systems and to elucidate the associated degradation and phase transformation mechanisms during repeated operation, but not to perform a comprehensive optimisation or screening of all possible molten salt compositions and loadings. Hence, salt compositions were selected that have been consistently reported to be effective, stable, and practically relevant in previous studies [34, 46], allowing meaningful

comparison with the existing literature while avoiding an excessively large compositional parameter space.

Two different concentrations of the SS promoted MgO were prepared using $NaNO_3$, keeping the molar ratio MgO: $NaNO_3$ equal to 1: 0.1 (10 mol%) and 1:0.05 (5 mol%). Similarly, DS-promoted MgO was prepared using a mixture of $NaNO_3$ and $NaNO_2$ keeping the molar ratio MgO: $NaNO_3$:$NaNO_2$ equal to 1:0.07:0.04 ($NaNO_3$ - 7 mol% and $NaNO_2$ - 4 mol %). Triple salt modification of MgO was conducted using a mixture of $LiNO_3$, $NaNO_3$ and $Na_2CO_3{\cdot}10H_2O$ (10 mol%) considering the molar ratio MgO:$LiNO_3$:$NaNO_3$:Na_2CO_3 equal to 1:0.02:0.076:0.004 ($LiNO_3$- 2 mol%, $NaNO_3$ - 7.6 mol% and Na_2CO_3 - 0.4 mol%). The hydromagnesite (HM) was initially calcined (Cal) in a horizontal tube furnace (1600°C capacity furnace, Sl. No.: 21-502145, Lenton Ltd., UK) at 600°C for 3h under 4L/min N_2 purge, followed by cooling it inside the furnace for 12 h. The cooled MgO was then stored in an air-tight 200 mL glass bottle.

Single salt–promoted (SS) MgO was prepared by dissolving 0.1078 g of $NaNO_3$ in 50 mL of methanol in a 200 mL glass bottle using a magnetic stirrer at 300 rpm for 10 min under a fume hood. Subsequently, 0.5013 g of MgO was added to the $NaNO_3$ solution, and the suspension was allowed to impregnate for 24 h at 600 rpm under ambient conditions (20 ± 2°C). The resulting mixture was then transferred to a 250 mL beaker, and most of the methanol was removed by evaporation in a preheated oil bath at 90°C until no free liquid was observed. The semi-dry solid was transferred to a glass Petri dish and dried in an oven at 105°C for 24 h. The obtained sample was stored in an airtight 50 mL centrifuge tube prior to CO_2 uptake testing. Double-salt (DS) and triple-salt (TS) modified MgO samples were prepared and stored following the same procedure. Photographs illustrating the synthesis steps for all samples are provided in Figs. S2–S4 (Supplementary Information).

2.2.2. CO_2 capture tests

CO_2 uptake was measured using a Q500 TA-TGA (TA instrument Q Series, England), varying the desorption temperature (500, 450, 400, and 380°C) and adsorption temperature (275, 300, 310 and 350°C), keeping the desorption and adsorption time fixed at 60 min and 240 min, respectively. Most of the literature suggests that molten salt–promoted alkaline earth metal oxides exhibit optimal CO_2 adsorption kinetics in the 200–400°C range (Qiao et al., 2017; Gao et al., 2017; Gao et al., 2022; Jo et al., 2017; Zhang et al., 2014; Pozzo et al., 2019; Zhao et al., 2018; Wang et al., 2025a). In practice, carbonation is typically performed at 275–350°C, while desorption is usually carried out at 400–450°C (Qiao et al., 2017; Wang et al., 2025b). In this study, a comprehensive range of temperatures for both adsorption and desorption was investigated, followed by cyclic CO_2 capture tests conducted at the optimized conditions. The investigation initially adopted literature-based temperature ranges and was subsequently extended to both lower and higher temperatures to fully assess performance.

For cyclical tests, 10-15 mg of sample was used. The desorption and adsorption tests were conducted, respectively, under 30 mL/min N_2 flow and 123 mL/min CO_2 (99.9% pure) flow from a compressed gas cylinder. It is acknowledged that in a practical CO_2 capture system the concentration will be lower; this is an initial scouting study to investigate degradation mechanisms; further work at lower concentrations, and in the presence of other impurities, is required. Employing pure CO_2 during the capture process minimizes interference from other gases and moisture, thereby allowing the intrinsic molten salt degradation mechanism to be established. The flow rate was selected to obtain the optimal uptake of CO_2 by maximising the quantity of CO_2 flowing through the TGA chamber without engendering noise within the results. An initial heating stage (with a rate of 10°C/min) was conducted under flow of N_2, this heating stage continued for the entire desorption duration including the time needed to reach the desired adsorption temperature. The CO_2 flow was started when the desired adsorption temperature reached, and it continued for the entire adsorption duration. Fig. S5 represents a typical heating and cooling cycles, showing mass change as a function of time. The CO_2 uptake (%) was determined using the formula in equation 4.

$$CO_2 \text{ uptake } (\%) = \frac{m_t - m_i}{m_i} \times 100 \quad (4)$$

In equation *iv* m_i= Mass of sorbent (g) after 1st desorption at a particular desorption temperature (e.g., 380, 400 and 450°C) and m_t = Mass of sorbent (g) kept for time t at a particular adsorption temperature (e.g., 275, 300, 310, 350°C) following the desorption.

Table 1 summarizes single CO_2 capture test conditions. Additionally, cyclical CO_2 capture tests were performed varying the number of cycles (5, 10, 20, and 22), desorption temperature (450, 400, and 380°C), adsorption temperature (300 and 310°C), and time for desorption (15 and 14 min) and adsorption (60, 20, 12, and 24 min). Although 14 vs. 15 minutes made little difference in practice, we used 15 min for the 60 min adsorption case to be conservative in ensuring complete desorption. Table 2 shows the cyclic CO_2 capture test conditions and sample identity (Table 1 presents all notations used in this study).

2.2.3. Characterization

X-ray diffraction (XRD Aeris, Malvern Panalytical, UK) was used to study the sorbent samples (with and without molten salt modification) before and after the cyclic tests. The diffractogram was recorded over a 2θ range of 20–70°, using a step size of 0.1° and a dwell time of 0.9 s per step. After conducting the X-ray scan, all diffractograms were analysed using ICDD pdf4+ for peak search and match, followed by Rietveld refinement using High Score plus.

The Rietveld refinement of the X-ray diffractograms was performed using search-and-match parameters based on the ICDD PDF-4 diffraction database within HighScore Plus. From the peak matching results, appropriate reference standard diffraction patterns (Section 3.4.2) corresponding to phases with known structural information were selected. Subsequently, in the refinement control tab, global parameters for all

Table 1
Summary of a single CO_2 capture test condition and sample identity.

Sample ID	Treatment	D. Temp.[a] (°C) and time (min)	A. Temp.[b] (°C) and time (min)
HM-Cal-D500-60-A300-240	No	500 and 60	300 and 240
HM-Cal-TS(0.1)-D500-60-A275-240	TS[c]	500 and 60	275 and 240
HM-Cal-TS(0.1)-D500-60-A300-240	TS	500 and 60	300 and 240
HM-Cal-TS(0.1)-D500-60-A350-240	TS	500 and 60	350 and 240
HM-Cal-TS(0.1)-D450-60-A300-240	TS	450 and 60	300 and 240
HM-Cal-TS(0.1)-D400-60-A300-240	TS	400 and 60	300 and 240
HM-Cal-DS(0.11)-D450-60-A300-240	DS[d]	450 and 60	300 and 240
HM-Cal-DS(0.11)-D400-60-A300-240	DS	400 and 60	300 and 240
HM-Cal-SS(0.1)-D450-60-A300-240	SS(0.1)[e]	450 and 60	300 and 240
HM-Cal-SS(0.1)-D400-60-A300-240	SS(0.1)	400 and 60	300 and 240
HM-Cal-SS(0.1)-D380-60-A310-240	SS(0.1)	380 and 60	310 and 240
HM-Cal-SS(0.05)-D400-60-A300-240	SS(0.05)[f]	400 and 60	300 and 240

[a] Desorption temperature;
[b] Adsorption temperature;
[c] A mixture of 0.02 molar ratio of $LiNO_3$ (2 mol%), 0.076 molar ratio of $NaNO_3$ (7.6 mol%) and 0.004 molar ratio of Na_2CO_3 (0.4 mol%);
[d] A mixture of 0.07 molar ratio of $NaNO_3$ (7 mol%) and 0.04 molar ratio of $NaNO_2$ (4 mol%);
[e] 0.1 molar ratio of $NaNO_3$ (10 mol%);
[f] 0.05 molar ratio of $NaNO_3$ (5 mol%). Irrespective of the temperature and time variation, desorption was conducted in N_2 flow with 30 mL/min and adsorption conducted in CO_2 flow with 123 mL/min

Table 2
Summary of cyclic CO_2 capture test condition and sample identity.

Sample ID	Cycle number	D. Temp. (°C) and time (min)	A. Temp. (°C) and time (min)
HM-Cal-SS(0.1)-D450-15-A300-60	5	450 and 15	300 and 60
HM-Cal-DS(0.11)-D450-15-A300-60	5	450 and 15	300 and 60
HM-Cal-SS(0.1)-D450-14-A300-20	10	450 and 14	300 and 20
HM-Cal-DS(0.11)-D450-14-A300-20	10	450 and 14	300 and 20
HM-Cal-SS(0.1)-D450-14-A300-12	10	450 and 14	300 and 12
HM-Cal-DS(0.11)-D450-14-A300-12	10	450 and 14	300 and 12
HM-Cal-TS(0.1)-D450-14-A300-12	10	450 and 14	300 and 12
HM-Cal-SS(0.1)-D450-14-A300-12	22	450 and 14	300 and 12[a]
HM-Cal-DS(0.11)-D450-14-A300-12	22	450 and 14	300 and 12[a]
HM-Cal-SS(0.1)-D400-14-A310-12	10	400 and 14	310 and 12
HM-Cal-SS(0.1)-D380-14-A310-12	10	380 and 14	310 and 12
HM-Cal-SS(0.1)-D380-28-A310-12	10	380 and 28	310 and 12
HM-Cal-SS(0.05)-D380-14-A310-12	10	380 and 14	310 and 12
HM-Cal-SS(0.05)-D400-14-A310-12	10	400 and 14	310 and 12
HM-Cal-SS(0.05)-D450-14-A300-12	10	450 and 14	300 and 12

[a] The adsorption time given doubled, i.e., 24 min at 11th and 22nd cycles.

phases were defined. In particular, the solver tolerance was set to 10^{-5}, error calculation was enabled, and the asymmetric peak function was specified as split width and shape within the phase profile.

A suitable parameter set function was then applied; in this case, the extended Rietveld function was selected to achieve the best fit to the diffractograms. Automatic fitting was performed, followed by phase quantification based on the lowest weighted profile residual (Rwp) value. To assess the reliability of the quantification, the goodness-of-fit (GoF) was evaluated for each diffractogram. If the GoF deviated significantly from unity, the search-and-match procedure and subsequent Rietveld refinement were repeated. It should be noted that this approach is statistical in nature and does not necessarily represent absolute gravimetric quantification. However, it is widely accepted as a semi-quantitative method for phase analysis in X-ray diffraction studies.

Additionally, an X-ray fluorescence study in the energy dispersive mode was conducted using an Epsilon 3 XRF spectrometer, Malvern Panalytical, UK, to judge the elemental composition, impurities, and contaminants in the sorbent samples.

Fourier Transform Infrared Spectroscopic (FTIR) study of the molten salt-promoted MgO before and after cyclic tests was performed using an Agilent Cary 630 FTIR Spectrometer. The spectrum for each sample was recorded after the summation of 32 scans within the wave number range 4000-400 cm^{-1}.

To determine the Na and Mg content in the molten salt-promoted MgO before and after the cyclic tests run, an inductively coupled plasma mass spectrometry (ICP MS) study was conducted using an Agilent ICP-MS 7900 analyser. Before performing ICP MS analysis, solid samples were digested using HNO_3 and HCl (10:1 molar ratio) in a PTFE container with a lid in a 3150 W microwave (CEM Matthews. NC, MARS 6 240/50, CEM Corporation, USA) for 20 min at 180°C. Following the digestion, the aliquot was diluted to 2% HNO_3 solution and one-tenth of the initial concentration by adding deionized water. Each sample was analysed with respect to a blank analysis prepared using the same concentration of acid.

The microstructures of SS-promoted MgO, before and after the cyclic CO_2 adsorption test at different desorption temperatures (380–450 °C), were examined using a JEOL JSM-6010LA scanning electron microscope (SEM) (JEOL Ltd., Japan). Microstructural images were recorded at an accelerating voltage of 20 kV and a magnification of 3 kX. Before the SEM analysis, the powder samples were mounted on SEM stubs using carbon tape and coated with a very thin layer of gold via sputtering.

2.2.4. *Thermodynamic analysis*

Thermodynamic modelling for the phase transformation and reaction equilibrium of the sodium nitrate-promoted sorbent was carried out using the computer program FactSage 8.0 (©FactSage Software and Databases, www.FactSage.com). FToxid and FactPS 8.0 data libraries were used for the thermodynamic calculations. The phase transformation and the possible product formation at the reaction equilibrium and their thermodynamic parameters were analysed to explore the potential of the molten salt's activity/degradation/conversion.

3. Results and discussion

3.1. *CO_2 capture test*

Fig. 1a represents the CO_2 capture performances of molten salt (with and without triple salt) -promoted MgO conducted at different adsorption temperatures (275, 300, and 350°C) keeping the desorption temperature constant at 500°C. From the figure, the unmodified MgO (No salt) possesses the lowest CO_2 capture capacity (<1%) compared to that of the other samples. The CO_2 adsorption test conducted at 300°C with 99.9% CO_2 for 240 min showed the best capacity and 275°C showed the least capacity among all temperatures. It is reported elsewhere that 300°C is the optimal temperature to maximise CO_2 adsorption capacity (Qiao et al., 2017). At lower temperatures, such as 275°C, the molten salt may not spread properly over the MgO surface, as this temperature is insufficient to form a melt phase. This limits the dissolution of [Mg^{2+}...O^{2-}] ion pairs in the melt phase, ultimately reducing the adsorption capacity (Gao et al., 2017; Gao et al., 2022; Zhang et al., 2014). However, at a very high adsorption temperature (350°C), the driving force for CO_2 adsorption decreases, most likely owing to the reduction in driving force for adsorption.

A temperature of 500°C is quite high for desorption and can damage the molten salts; therefore, the following tests were performed, reducing the desorption temperature. Figs. 1b-d depict the CO_2 adsorption capacity of different molten salts (SS, DS and TS)-promoted samples at different desorption temperatures (450 and 400°C in 30 ml/min N_2 flow) and different molar concentrations of SS keeping the adsorption temperature fixed at 300°C for 240 min. As shown in the figure, the CO_2 adsorption capacity of the SS-promoted sample increases with decreasing desorption temperature. A similar trend is observed for both DS- and TS-promoted MgO samples. The decrease in CO_2 capture capacity with increasing desorption temperature (Fig. 1b-c) is governed by the conversion of nitrate salts into their respective carbonates (as indicated by thermodynamic analysis) or their decomposition (as demonstrated by XRD) at higher temperatures. This, in turn, reduces the overall dispersion of the melt phase across the MgO surface and ultimately decreases CO_2 uptake (Gao et al., 2017; Pozzo et al., 2019).

The CO_2 uptake for SS-promoted MgO was observed to be 14.84 mol/kg (65.3 w/w%) at a desorption temperature of 380°C (graph not shown), which is slightly higher than that obtained at 400°C (14.73 mol/kg corresponding 64.8 w/w%) using the same sample and identical adsorption kinetics. Notably, an identical CO_2 adsorption capacity of 13.2 mol/kg (corresponding weight % is 58.1%) is observed for SS- and TS-promoted MgO at their respective desorption temperatures of 450°C and 400°C. However, when evaluated at 450°C, the TS-promoted sample exhibits the lowest CO_2 capture capacity (12.11 mol/kg corresponding to 53.3 w/w%) compared to that of SS- and DS-promoted samples under identical conditions. Overall, among the salt-modified MgO samples, SS-

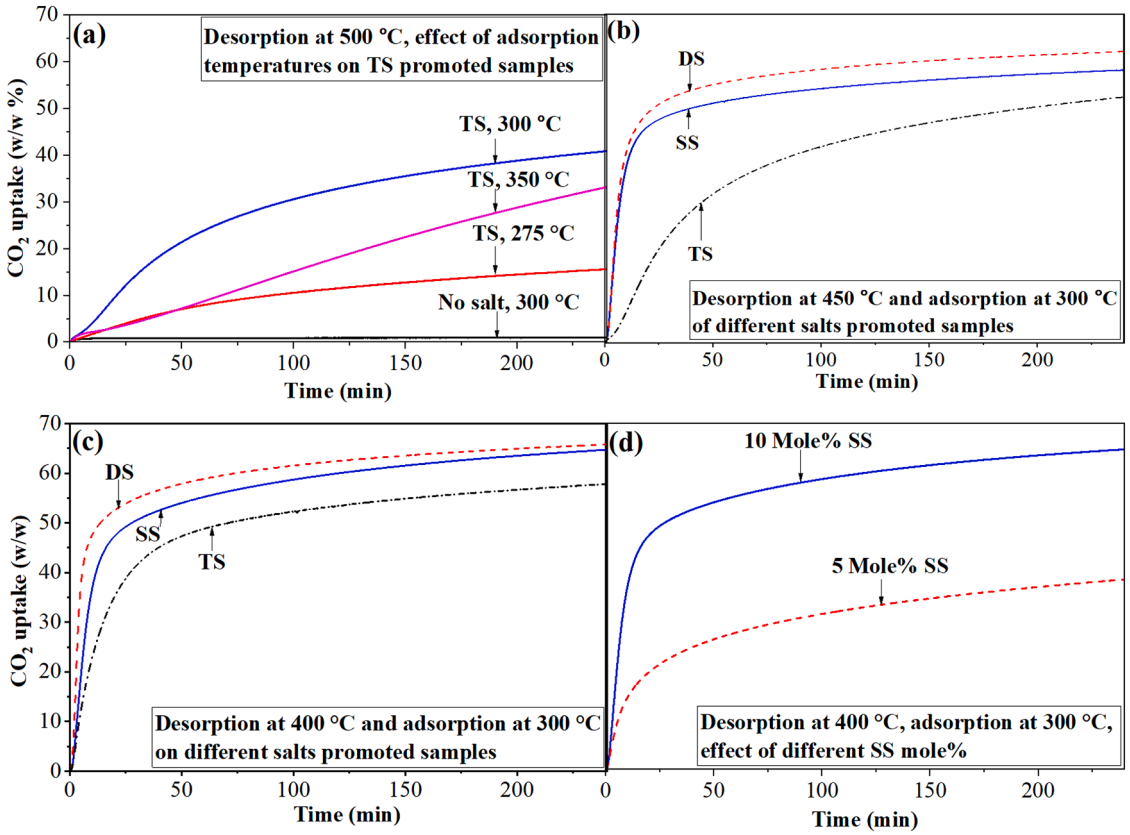


Fig. 1. **(a)** CO_2 capture performances of molten salt (without and with triple salt) promoted MgO conducted at different adsorption temperatures (275, 300, and 350°C) keeping the desorption temperature constant at 500°C, **(b)** CO_2 adsorption capacity of different molten salt (SS, DS and TS) promoted samples, desorption conducted at 450°C and adsorption at 300°C, **(c)** CO_2 capture capacity of different (SS, DS, and TS) promoted samples, desorption conducted at 400°C and adsorption at 300°C, **(d)** Effect of different molar concentrations (10 and 05%) on the CO_2 capture capacity of SS promoted sample, desorption done at 400°C and adsorption at 300°C.

and DS-promoted MgO demonstrate the best CO_2 capture performance, achieving adsorption capacities of 14.73 mol/kg (corresponding weight % is 64.84%) and 14.95 mol/kg (corresponding weight% is 65.8%), respectively, with the DS-promoted sample showing a slightly higher uptake at a desorption temperature of 400°C.

On the other hand, reduction in the quantity of the molten salt decreases CO_2 capture capacity as depicted in Fig. 1d. From the figure, the CO_2 capture capacity of the 5 mol% SS-promoted MgO sample is 8.7 mol/kg indicating that reducing the molten salt concentration by 50% (i.e., decreasing the MgO:$NaNO_3$ molar ratio from 0.1 to 0.05) results in a 40.9% decrease in CO_2 capture capacity. The difference in adsorption capacity observed in Fig. 1d can be attributed to the dilution effect. The dilution of molten salt content may reduce the formation of solvated ion pairs of MgO in the molten salt phase, limit the interaction of gaseous CO_2 with the MgO surface, and restrict the formation of triple-phase boundaries (Gao et al., 2017). Consequently, this may lead to a lower population of $MgCO_3$ precipitates.

3.2. Cyclic CO_2 capture test

3.2.1. Five cycle test, test condition: desorption 450°C for 15 min adsorption at 300°C for 60 min

Fig. 2a represents a five-cycle CO_2 capture test of SS(0.1) and DS (0.11) promoted samples. The desorption was performed at 450°C for 15 min, while adsorption was performed at 300°C for 60 min as summarised in Table 2. Table 3 presents the CO_2 capture capacity of all samples at the end of cyclical tests. The CO_2 adsorption capacities of both samples are found to be similar in the first cycle, followed by an increasing difference in adsorption capacity. At the end of the fifth cycle, the DS (0.11) promoted sample exhibits a higher adsorption capacity (32.5%) compared to the SS-promoted sample. The higher adsorption capacity of the DS(0.11) sample compared to the SS(0.1) sample at the end of the fifth cycle could be attributed to the presence of $NaNO_2$ (37%) in the DS sample, which has a higher proportion of melt phase due to its lower melting point (271°C), as well as a lower O^{2-} content. This composition likely allows more CO_2 interaction (resulting in faster reaction kinetics) with the bare MgO surface compared to the $NaNO_3$-promoted sample (Qiao et al., 2017; Gao et al., 2022).

The mass change at the end of the desorption cycle (i.e., the remaining mass after CO_2 has been desorbed) is lower for the DS(0.11)-promoted sample than for the SS(0.1) promoted sample (Fig. 2b), indicating mass loss from the solid / liquid particles. Additionally, the change in mass between the carbonated and uncarbonated states decreases as exposure time or number of cycles increases. This phenomenon can either due to the sintering of MgO over cyclic heating cooling or be attributed to the decomposition of molten salt, as confirmed by XRD analysis (see Section 3.4.2).

3.2.2. Ten cycle test, test condition: desorption 450°C for 14 min adsorption at 300°C for 20 min

Fig. 3 presents the results of a ten-cycle test for SS(0.1) and DS(0.11) promoted samples, with desorption conducted at 450°C for 14 min and adsorption at 300°C for 20 min. The trend observed is similar to that of the five-cycle test, with the DS-promoted sample revealing a higher CO_2 capture capacity up to the eighth cycle. However, beyond the eighth cycle, the CO_2 capture capacity of DS(0.11) declines, resulting in a lower adsorption capacity at the tenth cycle compared to the SS-promoted sample. A critical observation is that when the adsorption time was

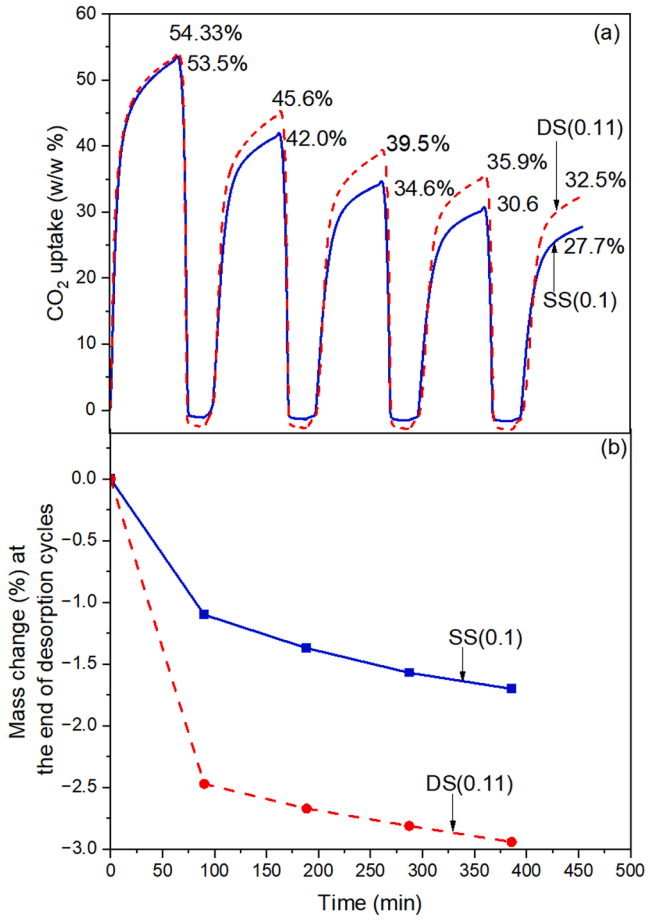


Fig. 2. (a) Five cycles CO_2 capture test behaviour of SS(0.1) and DS(0.11) samples conducted desorption at 450°C for15 min and adsorption at 300°C for 60 min, (b) Mass change (%) at the end of desorption cycles of SS(0.1) and DS (0.11) samples Vs. time.

maintained at 60 minutes (Fig. 2a), the DS-promoted sample exhibited only slightly higher adsorption than the SS-promoted sample during the first cycle. In contrast, when the adsorption time was reduced to 20 minutes (Fig. 3a), the DS-promoted sample showed a significantly higher uptake. In the subsequent cycles up to the eighth cycle, the DS-promoted samples desaturated more quickly and demonstrated faster CO_2 adsorption kinetics than the SS-promoted sample.

3.2.3. *Ten cycles test for different molten salts promotes samples keeping adsorption time at 12 min*

Analysing the ten-cycle test behaviour of different samples (SS(0.1), DS(0.11), and TS(0.1)-promoted MgO), which involved desorption at 450°C for 14 minutes and adsorption at 300°C for 12 minutes (Fig. 4a), it is observed that, similar to other cyclic tests, the DS-promoted sample exhibits the highest adsorption capacity during the initial cycles, up to five cycles, after which it decreases with increasing exposure time or cycle number. This may be because $NaNO_2$ melts at a lower temperature (Bond and Jacobs, 1966; Fei et al., 2019; Pacheco et al., 2002), rapidly becoming saturated with dissolved CO_2 and $[Mg^{2+}...O^{2-}]$ ion pairs compared to other molten salt compositions (Qiao et al., 2017; Gao et al., 2022). In contrast, a longer adsorption time (60 minutes and 20 minutes instead of 12 minutes as in Figs. 2a and 3) results in a higher adsorption capacity for the DS-promoted sample, compared to the shorter adsorption time (12 minutes in Fig. 4a). This can be explained by allowing more time for desaturation through the precipitation of $MgCO_3$ and the movement of reaction products away from the reaction site (Gao et al., 2017), which facilitates further CO_2 accumulation in the melt phase.

Table 3
Summary of CO_2 capture capacity at the end of cyclic tests and mass change (%).

Sample ID	No. of Cyclic test	CO_2 uptake at the end of cycles % and (mol/kg)	Mass change (%) at the end of final desorption cycle
HM-Cal-SS(0.1)-D450-15-A300-60	5	29.39 (6.68)	-1.69
HM-Cal-DS (0.11)-D450-15-A300-60	5	35.41 (8.05)	-2.91
HM-Cal-SS(0.1)-D450-14-A300-20	10	17.93 (4.08)	-1.62
HM-Cal-DS (0.11)-D450-14-A300-20	10	19.23 (4.37)	-1.23
HM-Cal-SS(0.1)-D450-14-A300-12	10	18.70 (4.25)	-1.60
HM-Cal-DS (0.11)-D450-14-A300-12	10	08.34 (1.89)	-1.24
HM-Cal-TS(0.1)-D450-14-A300-12	10	17.29 (3.93)	-1.45
HM-Cal-SS(0.1)-D450-14-A300-12[a]	22	13.03 (2.96)	-2.53
HM-Cal-DS (0.11)-D450-14-A300-12[a]	22	04.99 (1.13)	-1.74
HM-Cal-SS(0.1)-D400-14-A310-12	10	20.91 (4.75)	-0.98
HM-Cal-SS(0.1)-D380-14-A310-12	10	18.02 (4.10)	9.52
HM-Cal-SS(0.1)-D380-28-A310-12	10	21.15 (4.81)	-4.32
HM-Cal-SS (0.05)-D380-14-A310-12	10	16.04 (3.65)	13.58
HM-Cal-SS (0.05)-D400-14-A310-12	10	15.08 (3.42)	-1.12
HM-Cal-SS (0.05)-D450-14-A300-12	10	15.00 (3.41)	-1.68

[a] The adsorption time given doubled, i.e., 24 min at 11th and 22nd cycles

On the other hand, the SS-promoted sample performs relatively better with a shorter adsorption time, demonstrating a better adsorption capacity after the tenth cycle (Fig. 4b), surpassing both the DS and TS-promoted samples. However, it shows a lower CO_2 adsorption capacity than the DS-promoted sample during the initial cycles.

The TS-promoted sample initially exhibits a low CO_2 adsorption capacity, potentially owing to its lower nitrate content compared to the SS and DS-promoted samples. However, its adsorption capacity becomes comparable to that of the SS-promoted sample after the fourth cycle. This could possibly be attributed to the retention of a similar amount of molten salt, particularly $NaNO_3$, in both the SS and TS-promoted samples after the fourth cycle. Fig. 4c illustrates the mass change percent after the desorption cycle for different samples over ten cycles. The graph displays that the SS-promoted sample possesses a higher mass change (more negative mass change%) compared to the DS and TS-promoted samples.

3.2.4. *Twenty-two cycles test for different samples with the 11th and 22nd cycles adsorption time doubled*

Fig. 5 presents the twenty-two-cycles CO_2 adsorption and desorption

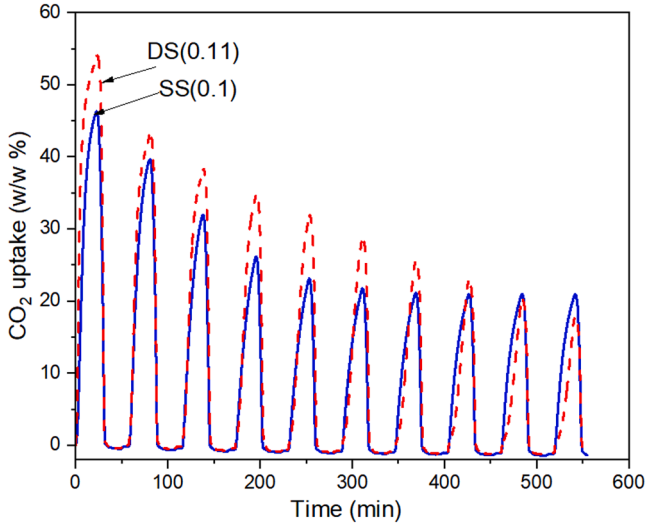


Fig. 3. Ten-cycles test of SS(0.1) and DS(0.11) samples, desorption conducted at 450°C for 14 min and adsorption at 300°C for 20 min.

test results for the SS(0.1) and DS(0.11) samples. Desorption was conducted at 450°C for 14 min, while adsorption occurred at 300°C for 12 min up to the 10th cycle and from the 12th to 21st cycle. For the 11th and 22nd cycles, the adsorption time was doubled to 24 min to assess whether this enhanced CO_2 capture capacity. The cyclic test graph reveals that, similar to the previous ten-cycle test, the DS-promoted sample exhibits a higher adsorption capacity up to the 5th cycle than the SS(0.1), followed by a decline through the 10th cycle. Increasing the CO_2 adsorption duration at the 11th cycle resulted in a higher CO_2 capture capacity for the DS(0.11) sample (24.4%) compared to the SS(0.1) sample (21.1%). However, beyond the 11th cycle, the adsorption capacity of both samples gradually declines. By the 22nd cycle, the DS (0.11) sample exhibits a lower adsorption capacity (12.82%) than the SS (0.1) sample (16.1%), even with the extended adsorption time (24 min).

3.2.5. Ten cycles test for SS-promoted sample at different desorption temperatures

To assess the impact of desorption temperature on the cyclical test performance, three different desorption temperatures were considered and compared. Fig. 6a illustrates the ten-cycle test behaviour of SS-promoted MgO, with desorption conducted at 450, 400, and 380°C for 14 min and adsorption at 300 and 310°C for 12 min. Note that for desorption temperatures of 400°C and 380°C, the adsorption temperature was 310°C, while for a desorption temperature of 450°C, the adsorption temperature was 300°C. The results indicate that the CO_2 capture capacity of the SS-promoted sample tested at a desorption temperature of 400°C and an adsorption temperature of 310°C is superior to that of the other desorption conditions (450 and 380°C). In the first cycle, the sample tested at 450°C shows a slightly higher capture capacity. However, from the subsequent cycles onward, the sample tested at 400°C dominates the CO_2 adsorption performance up to the tenth cycle.

Fig. 6b presents the variation in maximum CO_2 adsorption (w/w%) at the end of each cycle over time for SS-promoted samples tested at different desorption and adsorption temperatures. Regardless of the cycle number, the sample subjected to 400°C desorption and 310°C adsorption consistently exhibits a higher adsorption capacity (except the first cycle) than those tested at 450 and 380°C. Notably, after ten cycles at 400°C desorption, the SS-promoted MgO retains a CO_2 capture capacity of 20.9%, whereas the capacities after ten cycles at 450 and 380°C desorption are measured at 18.6% and 18.0%, respectively.

A critical analysis of the cyclical test conducted on the SS-promoted sample at a desorption temperature of 380°C reveals a significantly

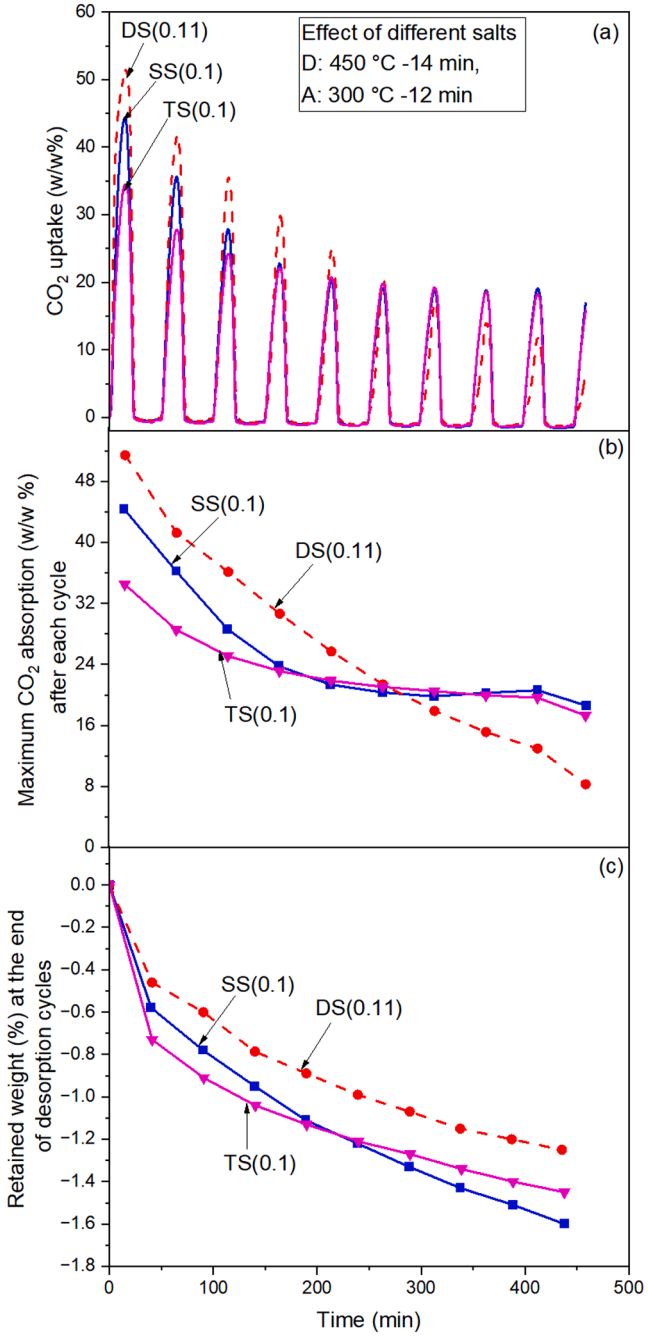


Fig. 4. (a) Ten-cycles test behaviour of SS(0.1), DS(0.11) and TS(0.1) promoted MgO samples, desorption conducted at 450°C for 14 min and adsorption at 300°C for 12 min, (b) Variation of maximum CO_2 adsorption (w/w%) after each cycles of SS(0.1), DS(0.11) and TS(0.1) promoted MgO samples with time, (c) Mass change (%) at the end of desorption cycles of SS(0.1), DS(0.11) and TS (0.1) promoted MgO samples Vs. time.

different behaviour compared to the other samples (Fig. 6a). As shown in Fig. 6c, the mass change (%) remains higher than zero (the CO_2 uptake percentage for SS-promoted MgO does not reach zero) during desorption at 380°C, indicating that a slower desorption of $MgCO_3$ molecules delays the regeneration of MgO. Notably, the percentage of mass change increases up to the fifth cycle before declining.

A different phenomenon of not achieving full calcination after desorption in the CO_2 capture test (up to the fifth cycle), conducted at a desorption temperature of 380 °C for the SS(0.1)-promoted sample (Fig. 6a and c), could be attributed to the incomplete decomposition of

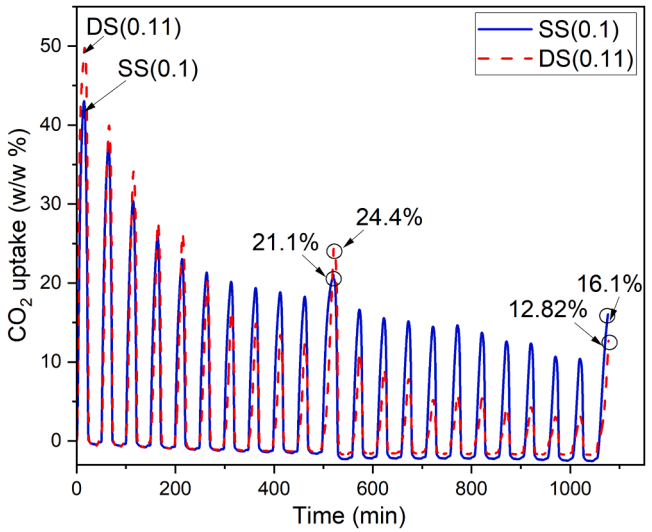


Fig. 5. Twenty two-cycles CO_2 adsorption and desorption test of SS(0.1) and DS(0.11) samples conducted desorption at 450°C for 14 min and adsorption at 300°C for 12 min up to 10th cycle and from 12th cycle to 21st cycle, the adsorption time was doubled, i.e., 24 min, for eleventh and twenty-second cycle.

$MgCO_3$ molecules within the core region of microparticle agglomerates and pore clogging caused by molten phases (Qiao et al., 2017). Decrease in mass change beyond the fifth cycle may result from the gradual decomposition of the molten salt due to prolonged exposure. A mechanism has been proposed in Section 3.4.

3.2.6. Ten cycles test of SS-promoted MgO at 380°C maintaining the desorption time doubled

Fig. 7a depicts the ten-cycle CO_2 capture test results for SS-promoted MgO, with desorption conducted at 380°C for 14 and 28 minutes while maintaining a constant adsorption condition at 310°C for 12 minutes. The figure shows that increasing the desorption time to 28 minutes leads to a significantly smaller CO_2 uptake after multiple desorption cycles. Fig. 7b presents the mass change percentage at the end of the desorption cycles as a function of exposure time. The weight loss indicates a loss of the sorbent, likely resulting from the decomposition of molten salt (Zhang et al., 2014) when the sorbent is exposed to a high temperature (380°C) for an extended period.

Fig. 8 depicts a possible physical mechanism underlying the critical behaviour of $NaNO_3$-promoted MgO (HM-Cal-SS(0.1)-D380-14-A310-12) during cyclical testing at a desorption temperature of 380 °C. It highlights the presence of trapped CO_2 molecules in the sealed zone, attributed to the impregnation of molten salts into the pore structure. The figure also illustrates the effect of CO_2 partial pressure, which increases with temperature (see Section 3.3). Since $NaNO_3$ melts above 310°C (confirmed by thermodynamic analysis), the melt phase may penetrate the micro or nanopores at 380°C, effectively sealing local zones. Even if $MgCO_3$ decomposes, the relatively low CO_2 partial pressure at 380°C in these localized regions prevents its escape through the protective melt phase, which is already saturated with Mg^{2+} and CO_3^{2-} ion pairs (Gao et al., 2017). Numerous reports explain that sealed internal porosity during calcination of $CaCO_3$ leads to a self-generated CO_2 atmosphere inside the particle that can stop calcination before completion, leaving an unreacted carbonate core and enhancing particle densification by sintering and shell formation, pore blockage, and shrinkage (Qiao et al., 2017; Qian et al., 2023; Maya et al., 2018; Martinez et al., 2024). On the other hand, the tests conducted at higher desorption temperatures (400 and 450°C) demonstrate that trapped CO_2 can escape more easily (results shown in Fig. 6 and Table 3) due to the generation of high internal partial pressure. However, very high

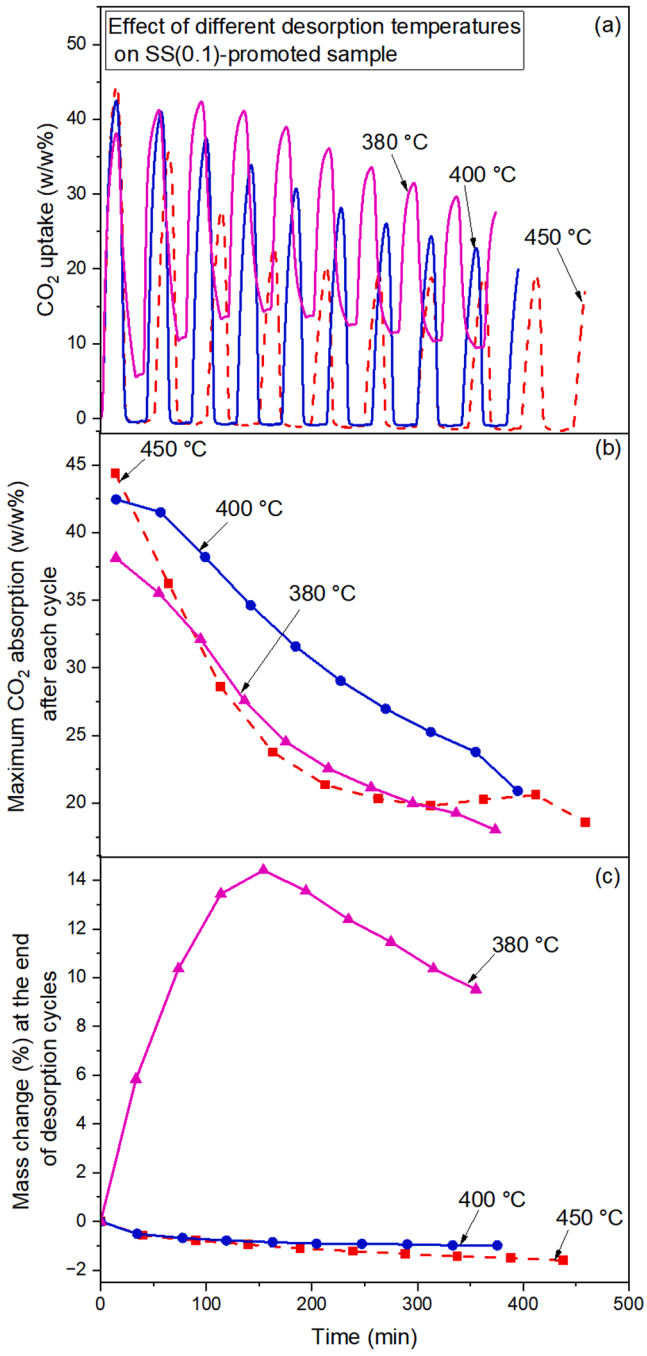


Fig. 6. (a) Ten-cycles test behaviour of SS-promoted MgO conducted desorption at 450, 400, and 380°C for 14 min and adsorption at 300 and 310°C for 12 min, (b) The variation in the maximum CO_2 adsorption (w/w%) of the SS-promoted sample after each cycle with the time tested at different desorption and adsorption temperatures, (c) Mass change (%) at the end of desorption cycles of the SS-promoted samples over time.

desorption temperatures may have adverse effects on the stability of the molten salts. Hence, a 400°C desorption temperature appeared to be optimal for SS-promoted MgO in cyclic CO_2 capture tests.

3.2.7. Dilution effect of SS ($NaNO_3$) concentration in the cyclic CO_2 capture performance

Fig. 9a shows the ten-cycle performance of 10 mol% and 5 mol% SS-promoted MgO samples, with desorption carried out at 400°C for 14 min and adsorption at 310°C for 12 min. Fig. 9b presents the maximum CO_2 capture capacity at the end of each adsorption cycle. The results

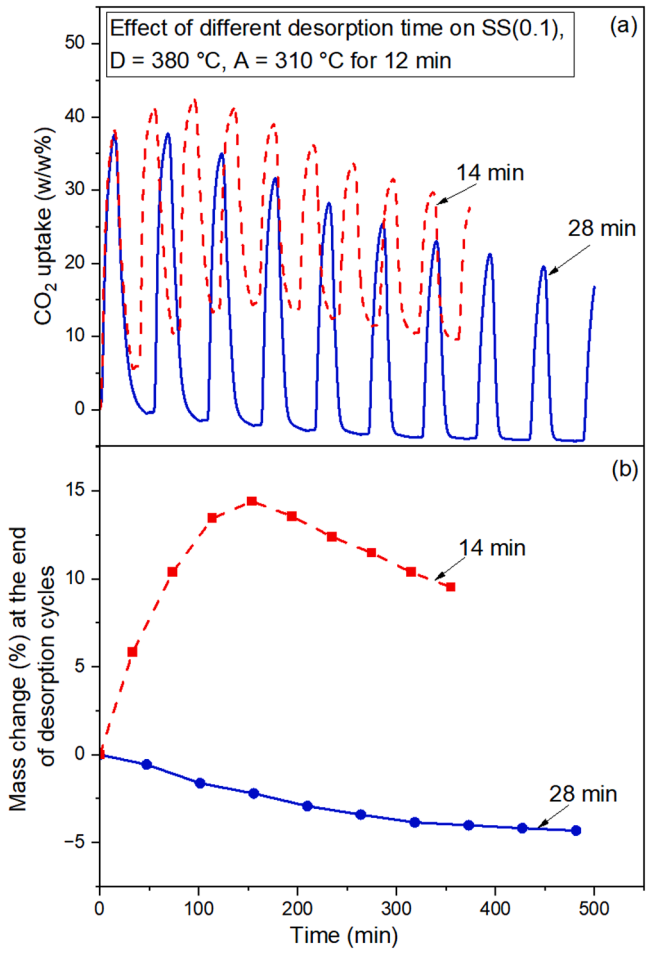


Fig. 7. (a) Ten-cycle CO_2 capture test graphs of SS(0.1)-promoted MgO, with desorption conducted at 380°C for 14 and 28 min, keeping the adsorption condition the same at 310°C for 12 min, (b) Mass change (%) at the end of desorption cycles as a function of time for the above samples, with desorption conducted for14 and 28 min at 380°C.

demonstrate that the CO_2 capture capacity of the 5 mol% SS-promoted sample is lower than that of the 10 mol% sample. This can be attributed to the reduced molten salt concentration, which decreases the triple-phase boundary (TPB) population at the solid–liquid–gas interface (Gao et al., 2017), eventually, leading to a reduced CO_2 capture performance.

The CO_2 capture capacity of the 10 mol% SS-promoted sample decreases by 50.7% from the first to the tenth cycle, whereas the 5 mol% sample shows a comparatively smaller reduction of 24.9%. Fig. 9c illustrates the percentage mass change at the end of the desorption cycles as a function of exposure time. Both samples exhibit similar mass change behaviour up to the sixth cycle; however, beyond this point, the 5 mol% sample shows a more rapid decline. The lower mass change (%) of SS (0.05)-promoted MgO compared to SS(0.1)-promoted MgO (Fig. 9c) is attributed to the greater decomposition of 5 mol% $NaNO_3$ relative to 10 mol% $NaNO_3$. This behaviour can be explained by the thinner distribution of the salt over the $MgCO_3$ surface (Choudhary et al., 2025), which facilitates faster evaporation and consequently leads to a reduction in CO_2 capture capacity.

3.3. Thermodynamic analysis

Fig. 10a illustrates the phase diagram of the $MgCO_3$-$NaNO_3$ mixture over the temperature range of 200–500°C, analysed using FactSage 8.0 (FactSage Software and Databases) with the FToxid database. Initially, the gas phase is not considered to allow an approximate understanding of the phase behaviour with temperature. The phase diagram indicates that $NaNO_3$ remains intact in the mixture up to 266°C, after which, it begins to partially transform into sodium carbonate, even though it does not melt until 310°C. Above this temperature, a mixture of sodium carbonate and molten $NaNO_3$ forms within the system, which ultimately enhances CO_2 capture capacity.

Given the high $MgCO_3/(MgCO_3 + NaNO_3)$ ratio of 0.9090 used in this study, the phase diagram predicts the presence of MgO, $MgCO_3$, and Na_2CO_3 below 400°C. This would imply that all $NaNO_3$ converts to Na_2CO_3; however, in practice, after ten cycles, nearly 50% of the total $NaNO_3$ remains in the system, as demonstrated by XRD analysis and Rietveld refinement (section 3.4.2). If complete $NaNO_3$ conversion had occurred, the $NaNO_3$-promoted sample would exhibit behaviour similar to that of calcined only MgO (Fig. 1a), but this is not observed. Cyclical tests results reveal that even after ten cycles, the SS-promoted sample retains a CO_2 capture capacity of 18–21%, regardless of the desorption conditions. This suggests the presence of a certain amount of SS in the sorbent, a finding further supported by XRD and Rietveld refinement.

The conversion of $NaNO_3$ to Na_2CO_3 is expected to result in substantial mass loss during the desorption cycles. Specifically, one mole of $NaNO_3$ yields only 0.5 mol of Na_2CO_3, corresponding to a theoretical mass loss of 37.64% relative to the molar mass of $NaNO_3$. This translates to an overall mass loss of 6.66% relative to the total mass of SS (10 mol% $NaNO_3$) promoted MgO, as calculated from equations S(i)–S(iv) (in the

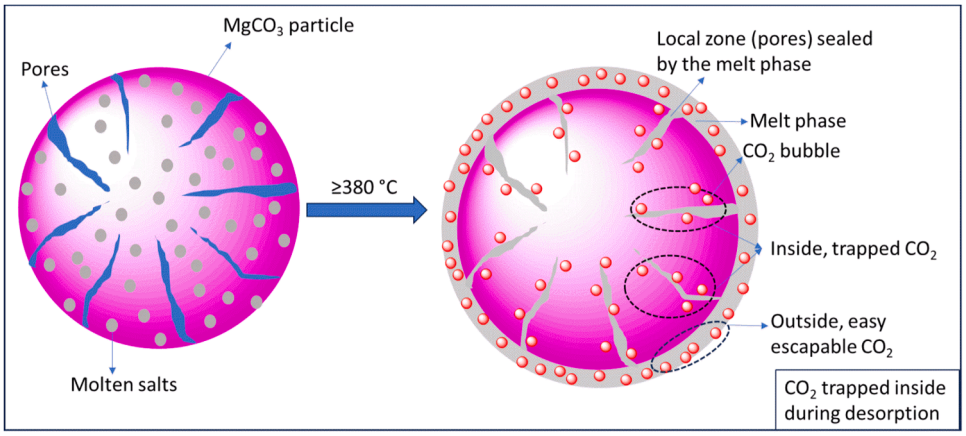


Fig. 8. Plausible mechanisms for explaining the critical behaviour of SS-promoted MgO (HM-Cal-SS(0.1)-D380-14-A31012) tested cyclically at 380°C desorption temperature. Due to the relatively low partial pressure of CO_2 around the particles' pores during desorption at 380°C, CO_2 molecules inside the capillaries are trapped.

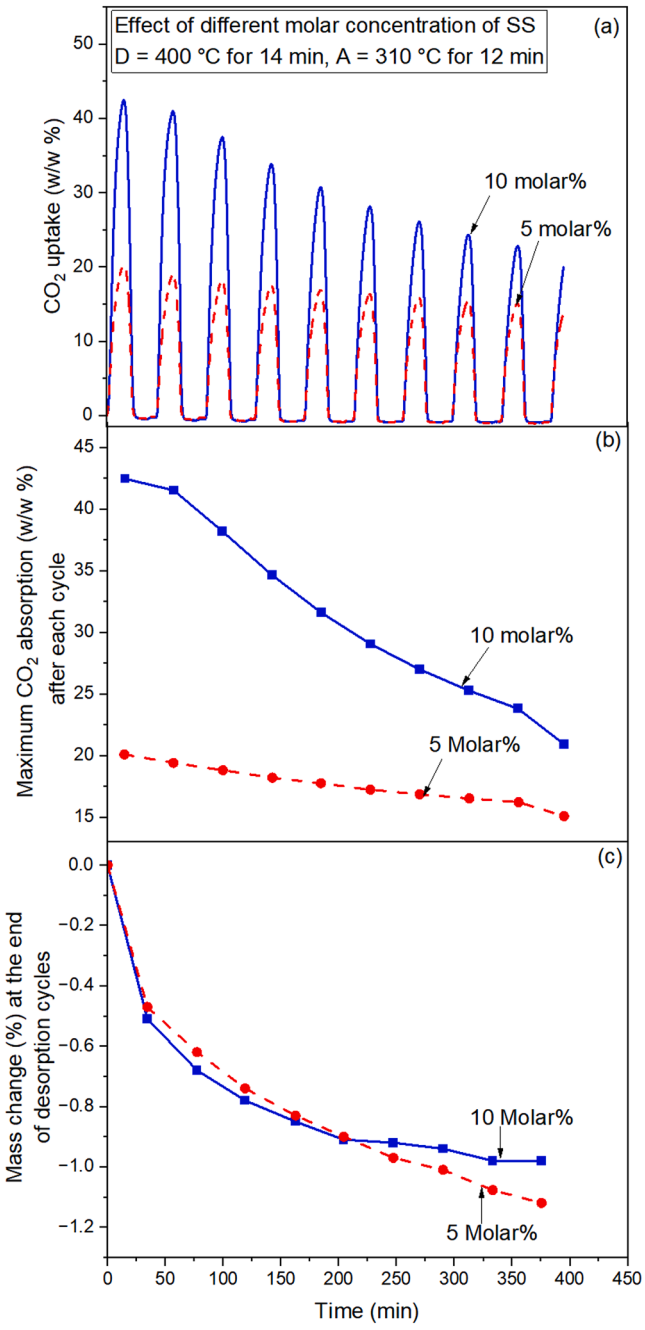


Fig. 9. (a) Ten-cycles test behaviour of 10 mol% and 5 mol% SS-promoted MgO samples conducted desorption at 400°C for 14 min and adsorption at 310°C for 12 min, (b) The variation of the maximum CO_2 capture capacity after the completion of each adsorption cycle with time, (c) Mass change (%) at the end of desorption cycles as a function of time.

Supplementary Information). Notably, this theoretical value is significantly higher than the mass change observed experimentally after desorption cycles.

If the mass loss of the SS-promoted samples arises entirely from the conversion of $NaNO_3$ to Na_2CO_3, the calculated conversion ratios (Table S1, Supplementary Information) indicate that the highest conversion ratio (64.86%) occurs for the sample subjected to a longer desorption period (28 min) at 380°C. In addition, dilution of the SS loading from 10 mol% to 5 mol% promotes the conversion, with the 5 mol% SS-promoted MgO exhibiting a conversion of 46% at 450°C. Although the thermodynamic analysis and mass-change data suggest conversion of $NaNO_3$ to Na_2CO_3, these results are not confirmed by XRD analysis. While the phase diagram of the $MgCO_3$-$NaNO_3$ mixture cannot predict kinetic limitations, it does indicate the formation of a molten phase beyond 310°C during desorption, which may play a role in influencing the CO_2 capture capacity of MgO.

For adsorption, the phase diagram analysis (Fig. 10b) using FactSage at 300°C shows that a mixture of 100 mol% MgO with less than 35 mol% $CO_2/(CO_2 + NaNO_3)$ contains both solid $NaNO_3$ and Na_2CO_3. However, as the CO_2 mole fraction increases, all $NaNO_3$ molecules transform into solid Na_2CO_3. Additionally, all MgO molecules transform into $MgCO_3$ when the $MgO/(MgO + CO_2)$ mole fraction falls below 50%. A similar phase diagram is observed for this three-component mixture at 310°C (Fig. 10c). However, in this case, all $NaNO_3$ phases appear in the liquid state. This suggests that 310°C is the optimal temperature for $NaNO_3$ melt-phase formation (Fei et al., 2019), which can enhance CO_2 accumulation. Fig. 10d presents the thermodynamic properties (ΔH, ΔS, and ΔG) of the reaction at different temperatures per mole of $MgCO_3$. Basic calculations of the partial pressure of CO_2 above MgO, utilising the NASA Glenn database (McBride et al., 2002) indicate that for the MgO / $MgCO_3$ / CO_2 system, the partial pressure of CO_2 above which $MgCO_3$ forms increases from 0.2 bar to 2.4 bar to 4.1 bar with an increase in temperature from 310 to 380 to 450°C. The increase in temperature enhances the driving force for desorption.

3.4. *Justification of the cyclic CO_2 test behaviour by characterisations*

The preceding sections indicate that the CO_2 capture capacity of molten salt-promoted commercial MgO declines with increasing cycle numbers/exposure time, regardless of the molten salt composition, concentration, or test conditions. This decline could be attributed to the loss of molten salts or sintering of the MgO sorbent. This section presents the results of ICP-MS, XRD, and FTIR analyses to further investigate and correlate these findings with the observed phenomena.

3.4.1. *ICP-MS analysis*

To assess the degradation of molten salt, ICP-MS analysis was performed on 10% $NaNO_3$-promoted MgO before and after ten cycles of testing. Table 4 presents the measured concentrations of Na and Mg in various acidic medium dilutions. Additionally, the atomic weight ratio of Mg to Na was calculated based on these values. The concentrations of Mg and Na vary with solvent dilutions. However, regardless of the dilution, the atomic mass ratio of Mg to Na remains unchanged at 1:0.12 before and after the cyclic tests. The Mg:Na atomic mass ratio for SS-promoted MgO closely matches the theoretical value (Mg:Na = 0.1) used for sample synthesis. Minor deviations may arise due to moisture content, atmospheric CO_2 exposure, and impurities in the commercial MgO.

Upon reviewing the ICP-MS analysis (Table 4), it is evident that the sodium content (Mg:Na) in the $NaNO_3$-promoted MgO remains constant even after ten cycles of CO_2 capture tests. Therefore, nitrate decomposition is the only likely cause for the deterioration of CO_2 uptake. Additionally, it has been established that the nitrate form of the sodium salt is solely responsible for the development of the melt phase, which accelerates CO_2 accumulation on the bare MgO surface (Gao at al., 2017).

3.4.2. *XRD analysis*

Fig. 11a–f present the X-ray diffractograms of molten salt-promoted MgO before and after ten cycles of testing. To determine the chemical phases semi-quantitatively, Rietveld refinement was performed. Table 5 provides the search and match conditions, along with the ICDD PDF selection for different phases. Figs. S6–S17 display all X-ray diffractograms after Rietveld refinement using HighScore Plus (refer to the supplementary information). In the X-ray diffractograms of both molten salt-modified and unmodified samples, peaks at $2\theta = 36.8°$, 42.7°, and 62.1° correspond to MgO (Periclase, denoted as 'p'), while peaks at 32.6°, 42.9°, 53.9°, 66.3°, and 69.3° indicate the presence of $MgCO_3$

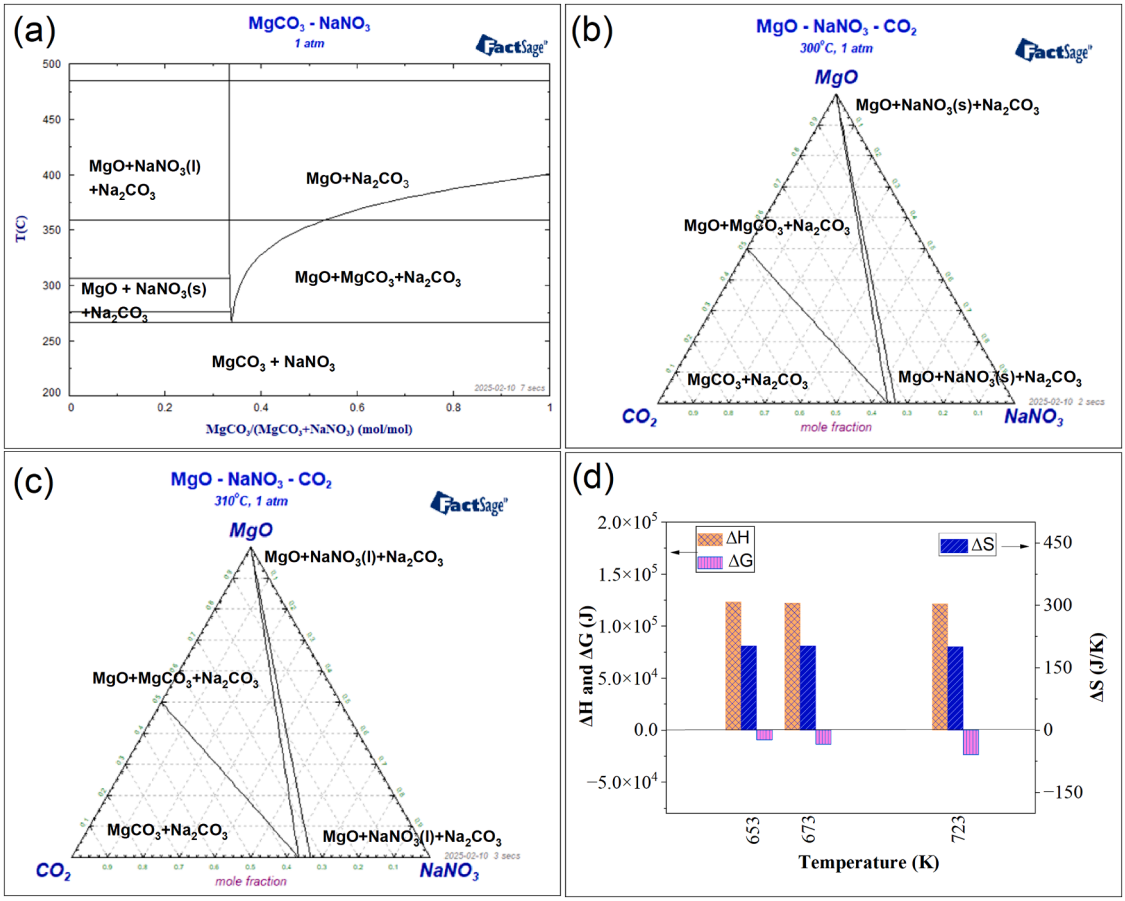


Fig. 10. (a) The phase diagram of the $MgCO_3$ and $NaNO_3$ mixture over the temperature range 200-500°C analysed using FactSage 8.0 (FactSage Software and Databases) with Ftoxid database, (b) Three-component phase diagram of MgO, $NaNO_3$ and CO_2 considering the situation during CO_2 adsorption at 300°C, (c) Three-component phase diagram of MgO, $NaNO_3$ and CO_2 considering the situation during CO_2 adsorption at 310°C, (d) The thermodynamic properties (ΔH, ΔS, and ΔG) of desorption at different temperatures per mole of $MgCO_3$.

Table 4
Summary of the ICP-MS analysis of 10% SS promoted MgO before and after the ten cycles of CO_2 capture test.

Sample	Dilution in HNO_3	Mg%	Na%	Mg: Na (atomic weight ratio)
HM-Cal-SS(0.1)	2.0%	88.69	9.87	1 : 0.117
	6.9%	88.39	10.37	1 : 0.123
HM-Cal-SS(0.1)- D400-14-A310-12	2.0%	86.76	10.04	1 : 0.122
	6.9%	88.04	9.96	1 : 0.119

(Magnesite, denoted as 'm') (Qiao et al., 2017; Gao et al., 2022). Peaks at $2\theta = 29.4°$, 31.9°, 35.4°, 38.9°, 47.9°, 48.3°, 55.6°, and 56.4° correspond to $NaNO_3$ (denoted as 'n'), while small peaks at 30.0°, 51.2°, and 58.8° are attributed to $NaNO_2$ (denoted as 'n_2') (Gao et al., 2022).

From the diffractograms (Fig. 11a), periclase (MgO) peaks appear broader in samples that have not undergone CO_2 capture testing (after calcination of the hydromagnesite), while magnesite peaks exhibit low intensity (appeared for SS and DS-promoted calcined hydromagnesite samples). Such findings may indicate sintering in the sample (since larger grains are associated with sharper peaks); unfortunately, we were unable to test this owing to the small quantities utilised in these experiments preventing retention for e.g. BET or BJH analysis. After the CO_2 capture test, the periclase peaks become sharper, and additional high-intensity magnesite peaks emerge (12b-f), indicating the conversion of MgO to $MgCO_3$. The effect of salt promotion is evident, as a minor magnesite peak is observed even before CO_2 capture testing in SS- and DS-promoted samples (Fig. 11a). Additionally, the intensity of sodium nitrate ($NaNO_3$) peaks decreases after ten cycles of CO_2 capture, suggesting partial decomposition.

Rietveld refinement of the X-ray diffractograms was performed following the procedure described in section 2.2.3 (Misture and Snyder 2001; Lee et al., 2014). This was conducted using search-and-match parameters based on the ICDD PDF-4+ diffraction database in High-Score Plus. Based on the peak matching results, the reference standard diffraction patterns (presented in Table 5) corresponding to phases with known structural information were selected. The phase composition of each sample is summarized in Table 6. As shown in the table, the initial $NaNO_3$ content in the SS(0.1) sample is 22.23%, but it decreases across all samples subjected to cyclic testing, regardless of test conditions and salt concentration. The decrease in $NaNO_3$ content after the cyclical tests through the Rietveld refinement confirms its decomposition. This decomposition causes weight loss during the desorption cycles, which ultimately reduces the CO_2 capture capacity as the number of cycles (exposure time) increases (Qiao et al., 2017; Zhang et al., 2014; Pozzo et al., 2019).

It is important to note that as the desorption temperature increases, the content of retained $MgCO_3$ (by weight) decreases, while the content of retained MgO (by weight) increases. This suggests that higher exposure temperatures increase the likelihood of molten salt decomposition, which in turn reduces the CO_2 capture capacity and results in a higher retention of MgO after completing the test cycles. Thermodynamic analysis predicts complete (100%) conversion of $NaNO_3$ to Na_2CO_3, while mass-change analysis based on thermodynamic considerations indicates a degree of conversion. However, the XRD results do not confirm this interpretation, as no diffraction peaks corresponding to

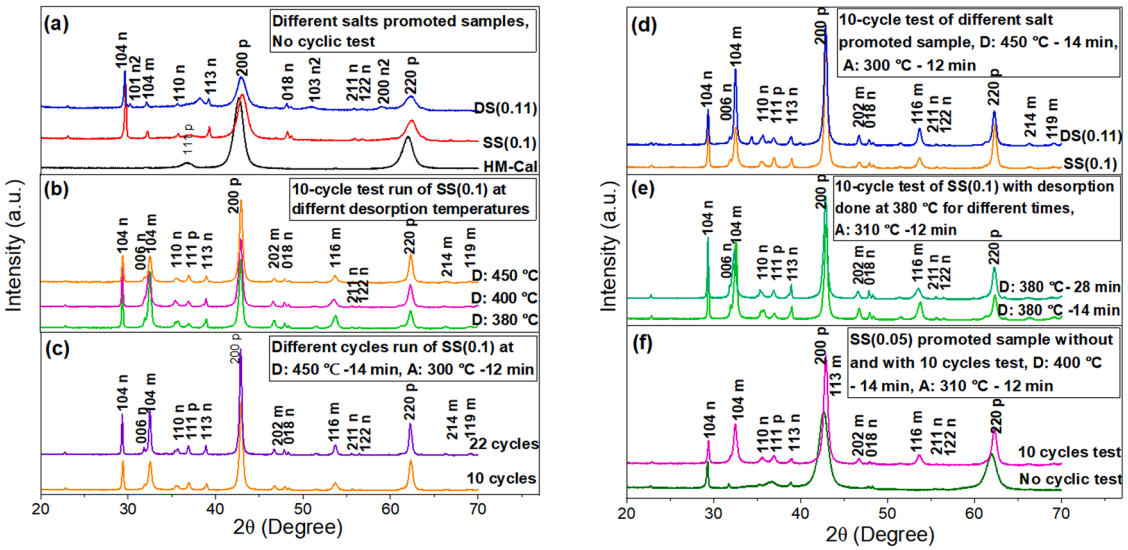


Fig. 11. XRD patterns of (a) different salts promoted samples that had not undergone cyclic test, (b) 10 cycles test run of SS(0.1) promoted sample at different desorption temperatures, keeping the desorption time 14 min and adsorption time 12 min, (c) 10 and 22 cycles run of SS(0.1) promoted sample, for 22 cycles test, the adsorption time kept 24 min for 11th and 22nd cycles. (d) XRD pattern of 10-cycles tested different molten salts promoted sample: SS(0.1) and DS(0.11), (e) 10 cycles tested SS(0.1) promoted samples, desorption run at 380°C for different time: 14 min and 28 min, (f) Without and with 10 cycles tested SS(0.05) promoted sample.

Table 5
ICDD reference code used to identify the chemical phases in X-ray diffractogram using ICCD pdf-4.

Phases	ICDD reference code	Notation used in this study
Magnesium oxide (periclase)	01-073-3815	p
Magnesium carbonate (magnesite)	04-014-4846	m
Sodium nitrate	01-079-2056	n
Sodium nitrite	01-087-1121	n2

Table 6
Weight percent of the chemical phases obtained by the Rietveld refinement of X-ray diffractograms.

Sample	Cycles run	Main Chemical phases (%)			
		MgO	$MgCO_3$	$NaNO_3$	$NaNO_2$
HM-Cal[a]	0	99.7	0.20	00.00	0.0
HM-Cal-SS(0.1)	0	77.7	0.00	22.3	0.0
HM-Cal-SS(0.05)[b]	0	92.0	0.00	07.2	0.0
HM-Cal-DS(0.11)	0	76.9	0.00	21.5	1.6
HM-Cal-SS(0.1)-D450-14-A300-12	10	49.0	38.7	12.2	0.0
HM-Cal-SS(0.1)-D400-14-A310-12	10	38.5	48.8	12.7	0.0
HM-Cal-SS(0.1)-D380-14-A310-12	10	25.9	61.6	12.5	0.0
HM-Cal-SS(0.1)-D380-28-A310-12	10	39.2	48.8	12.0	0.0
HM-Cal-SS(0.1)-D450-14-A300-12	22	45.0	42.6	12.1	0.0
HM-Cal-DS(0.11)-D450-14-A310-12	10	38.2	49.4	09.0	0.1
HM-Cal-TS(0.1)-D450-14-A300-12[c]	10	50.7	36.7	12.0	0.0
HM-Cal-SS(0.05)-D400-14-A310-12[d]	10	52.8	40.5	06.1	0.0

[a] Contains 0.1% CaO.
[b] Contains 0.7% Na_2CO_3.
[c] Contains 0.4% $CaCO_3$.
[d] Contains 0.5% $CaCO_3$.

Na_2CO_3 are detected. It is, of course possible that Na_2CO_3 is forming, but that it is amorphous.

3.4.3. FTIR analysis

Fig. 12 presents the FTIR spectra of calcined MgO and SS(0.1)-promoted samples before and after cyclic tests. A broad peak at 1418 cm^{-1}, observed in calcined hydro-magnesite (MgO), corresponds to the asymmetric stretching of the C–O bond in carbonates, attributed to CO_2 adsorption on MgO surfaces (Trivedi et al., 2015). The presence of a sharper peak at the same position in all other samples (except pure $NaNO_3$) indicates CO_2 chemisorption on MgO. Additionally, broad peaks at 1119 cm^{-1} and 852 cm^{-1} are observed in calcined MgO corresponding to the symmetric stretching and bending of the C–O bond in surface-adsorbed carbonates, respectively (Zahir et al., 2019; Wang et al., 2023). These peaks become more intense and well-defined in SS-promoted samples before and after cyclical tests, confirming active CO_2 capture. In the SS(0.1)-promoted MgO sample, a new peak at 1478

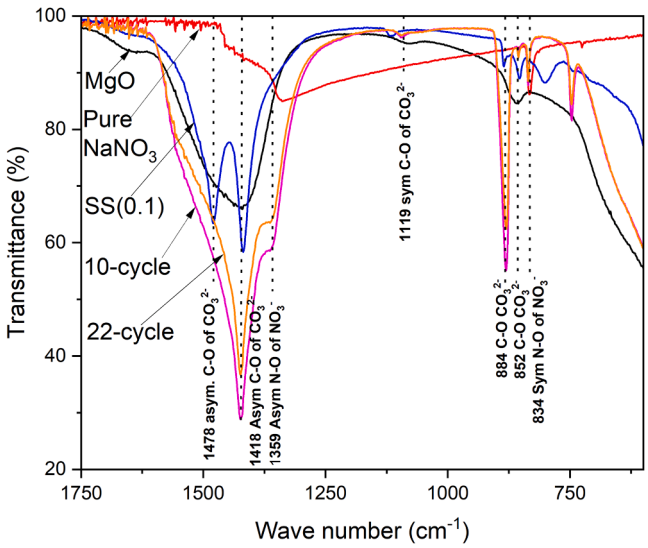


Fig. 12. FTIR spectra of MgO produced from hydromagnesite, pure $NaNO_3$, SS (0.1)-promoted samples, SS(0.1)-promoted sample after 10 and 22-cycle of CO_2 capture tests (denoted as 10-cycle and 22-cycle, respectively, in the figure).

cm^{-1} is observed due to the asymmetric stretching of the C–O bond in magnesite (Zahir et al., 2019), indicating enhanced CO_2 capture capacity facilitated by $NaNO_3$, as reported elsewhere (Qiao et al., 2017; Gao et al., 2017; Gao et al., 2022, Zhang et al., 2013; Chen et al., 2021).

Pure $NaNO_3$ and SS(0.1)-promoted samples exhibit a symmetric N–O stretching peak at 834 cm^{-1} (Zahir et al., 2019). Since $NaNO_3$ influences CO_2 adsorption on MgO surfaces even before any CO_2 capture test, SS (0.1)-promoted MgO does not show the asymmetric N–O stretching peak of NO_3^- at 1359 cm^{-1} (Zahir et al., 2019). However, after ten and twenty-two cycles of CO_2 capture tests, both pure $NaNO_3$ and SS-promoted MgO show a distinct asymmetric N–O stretching peak at 1359 cm^{-1}. This indicates that while $NaNO_3$ does not fully decompose, its content significantly decreases after cyclic tests, as evidenced by the reduced peak intensity of N–O stretching after ten and twenty-two cycles.

FTIR analysis (Fig. 12) reveals that the $NaNO_3$ peak remains even after ten and twenty-two cycles of the CO_2 capture test for SS-promoted MgO samples. However, a decrease in the intensity of the N-O peak of $NaNO_3$ is observed as the number of test cycles increases (from ten to twenty-two), indicating the decomposition of $NaNO_3$ with more cycles. Regarding the C-O peak intensities of CO_3^{2-} at 1418 cm^{-1} and 884 cm^{-1}, a higher amount of magnesite is exhibited after the cyclical test.

3.4.4. Microstructure analysis

Fig. 13 illustrates the microstructural images of SS-promoted MgO before and after the cyclical CO_2 capture tests conducted at various desorption temperatures (380–450 °C). The SEM image of the fresh SS-promoted MgO (Fig. 13a) reveals a rosette-like structure, attributed to the mixing of sodium nitrate with the MgO particles. After ten cycles of CO_2 capture test, the particles of SS-promoted MgO become sintered, and the rosette-like structures are destroyed due to the decomposition of the composite structure, regardless of the desorption temperature. As the desorption temperature increases from 380 °C (Fig. 13b) to 400 °C (Fig. 13c) and then to 450 °C (Fig. 13d), the degradation of the rosette-like configuration becomes more pronounced and porous nature of the particles reduces. This structural breakdown and reduction in particle decoration eventually reduces the CO_2 capture capacity of SS-promoted MgO, leaving more unreacted MgO after the cyclic test at the higher desorption temperature (450 °C), as confirmed by XRD analysis.

It is important to note that the specific surface area (derived from the Brunauer–Emmett–Teller (BET) equation) and pore size distribution (calculated using the Barrett–Joyner–Halenda (BJH) method) are critical parameters for elucidating the mechanism behind the decline in CO_2 capture capacity over repeated cycles. Previous studies consistently report that fresh sorbents exhibit higher BET surface area and larger pore volumes, whereas cyclic CO_2 capture leads to a progressive reduction in pore volume and surface area (Qiao et al., 2017; Chen et al., 2021; Zhang et al., 2014). This deterioration is further exacerbated during high-temperature desorption (400–450°C), likely due to pore clogging caused by the molten state of metal nitrates (Qiao et al., 2017).

Consistent with these findings, the cyclic CO_2 capture tests conducted at 300°C (adsorption) and 400–450°C (desorption) in this study suggest a similar mechanism, as hypothesised in Fig. 8 (Section 3.2.6) and supported by XRD, FTIR, and microstructural analyses. Although BET measurements could not be performed due to limited sample quantity (~10 mg), the observed CO_2 capture performance of sodium nitrate–promoted samples aligns well with existing literature and is corroborated by complementary characterization techniques. It is acknowledged that BET analysis is an important component of future work when sufficient sample quantities become available.

It is important to note that high-resolution TEM mapping would enable direct visualization of the spatial distribution of alkali metal species within the MgO matrix, thereby providing deeper insight into the relationship between additive dispersion and CO_2 capture performance. However, this analysis has not been conducted at the present stage. We acknowledge this as a limitation of the current study and have explicitly identified it as an important direction for future investigation.

Hence, it can be conclusively stated that, irrespective of salt composition, the cyclic CO_2 capture performance of alkali metal nitrate–promoted MgO declines with increasing cycle number. This degradation is primarily attributed to sintering and/or structural degradation of the metal nitrate phase, leading to pore clogging, as evidenced by ICP-

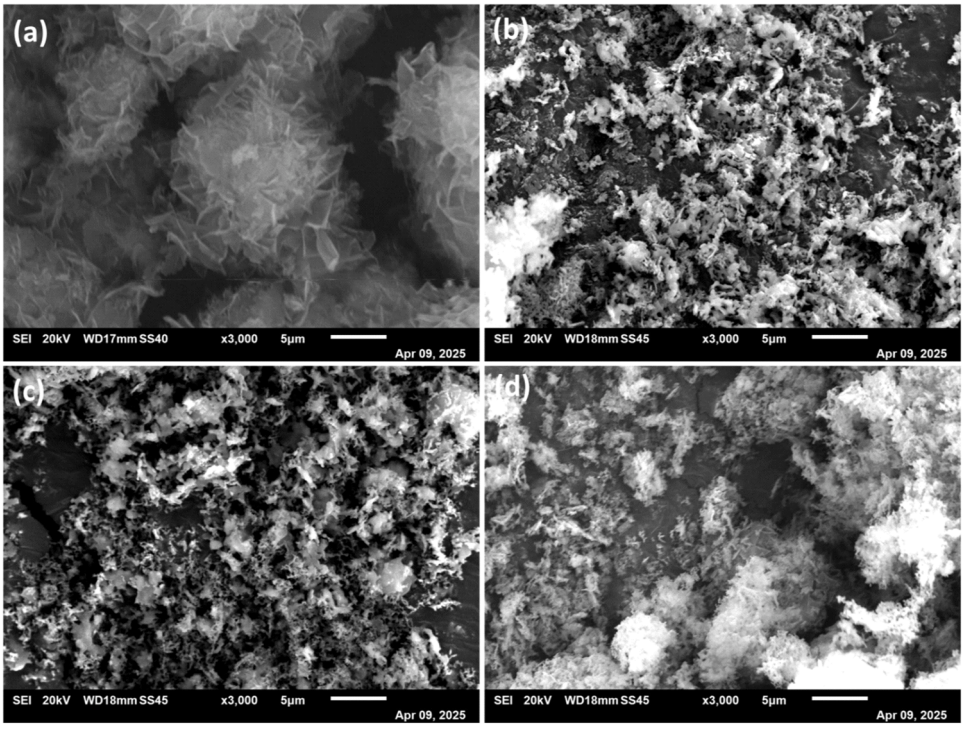


Fig. 13. SEM image of (a) fresh SS-promoted MgO, (b) SS-promoted MgO after 10-cycle test at D = 380°C, (c) SS-promoted MgO after 10-cycle test at D = 400°C, and (d) SS-promoted MgO after 10-cycle test at D = 450°C.

MS, XRD, FTIR, and SEM analyses.

4. Conclusions

This study investigated the cyclical CO_2 capture performance of molten salt–promoted commercial MgO sorbents using single, double, and triple-salt systems. Cyclic adsorption–desorption tests were conducted at adsorption temperatures of 300–310°C and desorption temperatures between 380 and 450°C.

The highest CO_2 capture capacity was obtained at an adsorption temperature of 300°C. At a desorption temperature of 400°C, single and double-salt–promoted MgO exhibited comparable capture capacities (~65%). Higher regeneration temperatures led to reduced performance, attributed to molten salt decomposition.

All sorbents showed a gradual decline in CO_2 capture capacity with increasing cycle number. The double-salt–promoted MgO performed better in the initial cycles, while the single-salt–promoted MgO demonstrated improved stability and higher capacity during extended cycling. Incomplete mass recovery during desorption at 380°C for the single-salt–promoted sample was associated with partial $MgCO_3$ decomposition and pore blockage.

The loss in cyclic performance was primarily attributed to the decomposition of nitrate-based molten salts, particularly $NaNO_3$. This was confirmed by XRD, Rietveld refinement, FTIR, and ICP-MS analyses, which indicated nitrate decomposition without significant loss of sodium content.

Data availability

All data supporting this study are provided in full in the paper.

Declaration of generative AI and AI-assisted technologies in the writing process

During the preparation of this work the authors used Open AI - ChatGPT in order to improve the readability of the manuscript. After using this tool, the authors reviewed and edited the content as needed and take full responsibility for the content of the published article.

CRediT authorship contribution statement

Sumit Chakraborty: Writing – review & editing, Writing – original draft, Visualization, Validation, Methodology, Investigation, Formal analysis, Data curation, Conceptualization. **Paul Fennell:** Writing – review & editing, Supervision, Resources, Project administration, Funding acquisition.

Declaration of competing interest

The authors declare that they have no known competing financial interests or personal relationships that could have appeared to influence the work reported in this paper.

Acknowledgement

The authors would like to gratefully acknowledge the funding agency EPSRC (EP/T033940/1) for their funding to pursue this research programme. The authors would like to thank Dr. David Danaci for his kind help and initial discussion of the research. Authors would like to thank Prof. Subrata Chakraborty, Centre Director, CCSID at IIEST Shibpur for advising and allowing facility to carry out the part of the investigation.

Supplementary materials

Supplementary material associated with this article can be found, in the online version, at doi:10.1016/j.ccst.2026.100633.

References

Abbasi, E., Hassanzadeh, A., Zarghami, S., Arastoopour, H., Abbasian, J., 2014. Regenerable MgO-based sorbent for high temperature CO_2 removal from syngas: 3. CO_2 capture and sorbent enhanced water gas shift reaction. Fuel 137, 260–268.

Adegoke, K.A., Tseki, P.F., 2025. Graphene-based metal-organic framework nanocomposites for CO2 reduction reactions. Carbon Capture Sci. Technol. 17, 100523.

Azmi, A., Aziz, M., 2019. Mesoporous adsorbent for CO_2 capture application under mild condition: a review. J. Environ. Chem. Eng. 7 (2), 103022. https://doi.org/10.1016/j.jece.2019.103022, 1-13.

Bhatta, L.K.G., Subramanyam, S., Chengala, M.D., Olivera, S., Venkatesh, K., 2015. Progress in hydrotalcite like compounds and metal-based oxides for CO_2 capture: a review. J. Clean. Prod. 103, 171–196.

Bond, B.D., Jacobs, P.W.M., 1966. The thermal decomposition of sodium nitrate. J. Chem. Soc. A 1966, 1265–1268. https://doi.org/10.1039/J19660001265. Accessed on 05/03/2025.

Bork, A.H., Ackerl, N., Reuteler, J., Jog, S., Gut, D., Zboray, R., Müller, C.R., 2022. Model structures of molten salt-promoted MgO to probe the mechanism of $MgCO_3$ formation during CO_2 capture at a solid–liquid interface. J. Mater. Chem. A 10, 16803–16812.

Cai, Y., Liu, W., Sun, Z., Yang, Y., Li, P., 2022. Granulation of alkaline metal nitrate promoted MgO adsorbents and the low-concentration CO_2 capture performance in the fixed bed adsorber. J. CO_2 Util. 61 (102047). https://doi.org/10.1016/j.jcou.2022.102047, 1-12.

Chen, J., Duan, L., Donat, F., Müller, C.R., 2021. Assessment of the effect of process conditions and material characteristics of alkali metal salt promoted MgO-based sorbents on their CO_2 capture performance. ACS Sustainable Chem. Eng. 9 (19), 6659–6672.

Choudhary, M.H., Chakraborty, N., Juglan, K.C., Syed, A.H., 2025. Temperature-dependent physicochemical interactions and spectroscopic characterization of sodium nitrate/sodium citrate in aqueous sodium salicylate solutions. Chemical Thermody. Therm. Anal. 18 (100176). https://doi.org/10.1016/j.ctta.2025.100176, 1- 22.

D'Alessandro, D.M., Smit, B., Long, J.R., 2010. Carbon dioxide capture: prospects for new materials. Angew. Chem., Int. Ed. 49 (35), 6058–6082. https://doi.org/10.1002/anie.201000431.

Dong, J., Wang, F., Chen, G., Wang, S., Ji, C., Gao, F., 2022. Fabrication of nickel oxide functionalized zeolite USY composite as a promising adsorbent for CO_2 capture. Chin. J. Chem. Eng. 46, 207–213.

Editorial, 2022. Climate change and human behaviour. Nat. Hum. Behav. 6 (11), 1441–1442. https://doi.org/10.1038/s41562-022-01490-9. Accessed on 05/03/2025.

Fei, Z., Zhang, Y., Ge, M., Wang, Y., Li, Y., Cheng, J., Wei, B., Hou, H., Liu, H., 2019. Probing thermal decomposition mechanism of molten nitrite/nitrates salt by time of flight mass spectrometry. Sol. Energy 183, 823–828.

Gao, F., Wang, S., Chen, G., Duan, J., Dong, J., Wang, W., 2020. A facile approach to the fabrication of MgO@Y composite for CO_2 capture. Adsorption 26, 701–709.

Gao, W., Xiao, J., Wang, Q., Li, S., Vasiliades, M.A., Huang, L., Gao, Y., Jiang, Q., Niu, Y., Zhang, B., Liu, Y., He, H., Efstathiou, A.M., 2022. Unravelling the mechanism of intermediate-temperature CO_2 interaction with molten-$NaNO_3$-salt-promoted MgO. Adv. Mater. 34 (2106677), 1-12.

Gao, W., Zhou, T., Gao, Y., Louis, B., O'Hare, D., Wang, Q., 2017. Molten salts-modified MgO-based adsorbents for intermediate-temperature CO_2 capture: a review. J. Energy Chem. 26, 830–838.

Gui, C., Wang, Z., Ling, C., Tang, Z., 2024. Molten salt-promoted MgO-based CO_2 adsorbents: selective adsorption on polycrystalline surfaces. J. Environ. Chem. Eng. 12 (2), 111972.

Harada, T., Hatton, T.A., 2015. Colloidal Nanoclusters of MgO coated with alkali metal nitrates/nitrites for rapid, high capacity CO_2 capture at moderate temperature. Chem. Mater. 27, 8153–8161.

Harada, T., Simeon, F., Hamad, E.Z., Hatton, T.A., 2015. Alkali metal nitrate-promoted high-capacity MgO adsorbents for regenerable CO_2 capture at moderate temperatures. Chem. Mater. 27 (6), 1943–1949. https://doi.org/10.1021/cm503295g.

Jin, S., Ho, K., Vu, A.T., Lee, C.H., 2017. Salt-composition-controlled precipitation of triple-salt-promoted MgO with enhanced CO_2 sorption rate and working capacity. Energy Fuels 31, 9725–9735.

Jo, S.I., An, Y.I., Kim, K.Y., Choi, S.Y., Kwak, J.S., Oh, K.R., Kwon, Y.U., 2017. Mechanisms of absorption and desorption of CO_2 by molten $NaNO_3$-promoted MgO. Phys. Chem. Chem. Phys. 19, 6224–6232.

Landuyt, A., Kumar, P.V., Yuwono, J.A., Bork, A.H., Donat, F., Abdala, P.M., Müller, C.R., 2022. Uncovering the CO_2 capture mechanism of NaNO3-promoted MgO by 18O isotope labeling. JACS Au 2, 2731–2741. https://doi.org/10.1021/jacsau.2c00461.

Lee, H.J., Kim, J.H., Kim, J.W., Cho, S.J., 2014. Structure transformation of Na-Mg based salts for CO_2 capture and storage at high temperature probed with variable temperature X-ray powder diffraction. Energy Procedia 63, 253–265.

Li, L., Zhang, B., Wang, F., Zhao, N., Xiao, F., Wei, W., Sun, Y., 2013. Study of the novel KMgAl sorbents for CO_2 capture. Energy Fuel 27, 5388–5396.

Li, Y.Y., Wan, M.M., Lin, W.G., Wang, Y., Zhu, J.H., 2014. A novel porous MgO sorbent fabricated through carbon insertion. J. Mater. Chem. A 2, 12014–12022. https://doi.org/10.1039/C4TA01188K.

Martinez, J., Wardini, J.L., Zheng, X., Moghimi, L., Rakowsky, J., Means, J., Guo, H., Kuzmenko, I., Ilavsky, J., Zhang, F., Dholabhai, P.P., Marais, L.D., Bowman, W.J., 2024. Precision calcination mechanism of $CaCO_3$ to high-porosity nanoscale CaO CO_2 sorbent revealed by direct in situ observations. Adv. Mater. Interfaces 11, 2300811.

Maya, J.C., Chejne, F., Gómez, C.A., Bhatia, S.K., 2018. Effect of the CaO sintering on the calcination rate of $CaCO_3$ under atmospheres containing CO_2. React. Eng. Kinetics Catal. 64 (10), 3638–3648.

Mayorga, S.G., Weigel, S.J., Gaffney, T.R., Brzozowski, J.R., 2001. Carbon dioxide adsorbents containing magnesium oxide suitable for use at high temperatures. US Patent 6280503B1. https://patents.google.com/patent/US6280503B1/en. Accessed on 05/03/2025.

McBride, B.J., Zehe, M., Gordon, S., 2002. NASA Glenn Coefficients for Calculating Thermodynamic Properties of Individual Species, NASA/TP—2002-211556. Glenn Research Center, Cleveland, Ohio. Available at https://ntrs.nasa.gov/citations/20020085330. Accessed on 20/10/2025.

Meinshausen, M., Meinshausen, N., Hare, W., Raper, S.C., Frieler, K., Knutti, R., Frame, D.J., Allen, M.R., 2009. Greenhouse-gas emission targets for limiting global warming to 2°C. Nature 458 (7242), 1158–1162.

Misture, S.T., Snyder, R.L., 2001. X-ray Diffraction. Encyclopedia of Materials: Science and Technology (Second Edition), pp. 9799–9808. https://doi.org/10.1016/B0-08-043152-6/01778-2. ISBN: 0080431526Available at https://www.sciencedirect.com/science/article/abs/pii/B0080431526017782. Accessed on 06/03/2025.

Modak, A., Jana, S., 2019. Advancement in porous adsorbents for post-combustion CO_2 capture. Microporous Mesoporous Mater. 276, 107–132.

Norouzpour, M., Santos, R.M., Chiang, Y.W., 2025. Activation methods for enhancing CO_2 mineralization via mine tailings - a critical review. Carbon Capture Science & Technology 15, 100430.

Olajire, A.A., 2013. CO_2 capture by aqueous ammonia process in the clean development mechanism for Nigerian oil industry. Front. Chem. Sci. Eng. 7 (3), 366–380. https://doi.org/10.1007/s11705-013-1340-7.

Pacheco, J.E., Showalter, S.K., Kolb, W.J., 2002. Development of a molten-salt thermocline thermal storage system for parabolic trough plants. J. Sol. Energy Eng. 124, 153–159.

Pozzo, A.D., Armutlulu, A., Rekhtina, M., Abdala, P.M., Müller, C.R., 2019. CO_2 uptake and cyclic stability of MgO-based CO_2 sorbents promoted with alkali metal nitrates and their eutectic mixtures. Appl. Energy Mater. 2 (2), 1295–1307.

Prashar, A.K., Seo, H., Choi, W.C., Kang, N.Y., Park, S., Kim, K., Min, D.Y., Kim, H.M., Park, Y.K., 2016. Factors affecting the rate of CO_2 absorption after partial desorption in $NaNO_3$-promoted MgO. Energy Fuel. 30, 3298–3305.

Qian, X., Qin, Y., Liu, Y., Hu, C., Wang, F., Hu, S., 2023. New insight into energy-saving calcination of limestone: preparation, characterization, and application of partially calcined limestone. ACS Sustainable Chem. Eng. 11, 16227–16239.

Qiao, Y., Wang, J., Zhang, Y., Gao, W., Harada, T., Huang, L., Hatton, T.A., Wang, Q., 2017. Alkali nitrates molten salt modified commercial MgO for intermediate-temperature CO_2 capture: optimization of the Li/Na/K ratio. Ind. Eng. Chem. Res. 56, 1509–1517.

Qin, Q., Wang, J., Zhou, T., Zheng, Q., Huang, L., Zhang, Y., Lu, P., Umar, A., Louis, B., Wang, Q., 2017. Impact of organic interlayer anions on the CO_2 adsorption performance of Mg-Al layered double hydroxides derived mixed oxides. J. Energy Chem. 26 (3), 346–353. https://doi.org/10.1016/j.jechem.2017.01.003.

Rochelle, G.T., 2009. Amine scrubbing for CO_2 capture. Science 325 (5948), 1652–1654. https://doi.org/10.1126/science.1176731.

Ruhaimi, A.H., Aziz, M.A.A., Jalil, A.A., 2021. Magnesium oxide-based adsorbents for carbon dioxide capture: current progress and future opportunities. J CO_2 Utili. 43, 101357–101378.

Ruminski, A.M., Jeon, K.J., Urban, J.J., 2011. Size-dependent CO_2 capture in chemically synthesized magnesium oxide nanocrystals. J. Mater. Chem. 21 (31), 11486–11491. https://doi.org/10.1039/c1jm11784j.

Shen, Y., 2023. Molten salt-mediated carbon capture and conversion. Fuel 339, 127473. https://doi.org/10.1016/j.fuel.2023.127473, 1-17.

Shi, Y., Zhao, Z., Li, H., Fan, X., Gao, X., 2026. Microwave-driven transformation of CO2 adsorbents regeneration: a comprehensive review from principles to system designs. Carbon Capture Sci. Technol. 19, 100602.

Stolaroff, J.K., Keith, D.W., Lowry, G.V., 2008. Carbon dioxide capture from atmospheric air using sodium hydroxide spray. Environ. Sci. Technol. 42, 2728–2735.

Trivedi, M.K., Branton, A., Trivedi, D., Nayak, G., Bairwa, K., Jana, S., 2015. Spectroscopic characterization of disodium hydrogen orthophosphate and sodium nitrate after biofield treatment. J. Chromatogr. Sep. Tech. 6 (5), 1000282. https://doi.org/10.4172/2157-7064.1000282, 1-5.

Vu, A.T., Park, Y., Jeon, P.R., Lee, C.H., 2014. Mesoporous MgO sorbent promoted with KNO_3 for CO_2 capture at intermediate temperatures. Chem. Eng. J. 258, 254–264.

Wang, Q., Cao, Z., Li, Q., Song, B., 2025a. Advances in concurrent CO_2 sequestration and heavy metal mobilization during fly ash carbonation: a review. Carbon Capture Sci. Technol. 17, 100519. https://doi.org/10.1016/j.ccst.2025.100519.

Wang, J., Feng, X., Wen, S., Zhan, D., Zhu, X., Ning, P., Zhang, Y., Mei, X.J.R., 2024. Recent advances in amine-functionalized silica adsorbents for CO_2 capture. Renewable Sustainable Energy Rev. 203, 114724, 1-24.

Wang, J., Huang, L., Yang, R., Zhang, Z., Wu, J., Gao, Y., Wang, Q., O'Hare, D., Zhong, Z., 2014a. Recent advances in solid sorbents for CO_2 capture and new development trends. Energy Environ. Sci. 7, 3478–3518.

Wang, Q., Luo, J., Zhong, Z., Borgna, A., 2011. CO_2 capture by solid adsorbents and their applications: current status and new trends. Energy Environ. Sci. 4, 42–55.

Wang, J., Huang, L., Yang, R., Zhang, Z., Wu, J., Gao, Y., Wang, Q., O'Hare, D., Zhong, Z., 2014b. Recent advances in solid sorbents for CO_2 capture and new development trends. Energy Environ. Sci. 7, 3478–3518. https://doi.org/10.1039/C4EE01647E.

Wang, W., Li, W., Huang, F., Zheng, C., Liu, T., Liu, C., 2023. Study on the application of two magnesium salts in low temperature adsorption refining of fragrant rapeseed oil. LWT - Food Sci. Technol. 188, 115399, 1-12.

Wang, Y., Niu, Y., Zhao, Y., Yu, B., Xu, J., Xu, Y., Yu, S., Bie, X., Li, Q., Zhang, Y., Ma, J., Sun, S., Song, F., Zhou, H., 2025b. Optimization and deactivation mechanisms of molten salt-promoted MgO for intermediate-temperature CO_2 capture. Carbon Capture Sci. Technol. 17, 100492.

Welton, C., Chen, F., Zhou, H.C., Yi, S., 2025. Mixed matrix membrane formation with porous metal–organic nanomaterials for CO2 capture and separation: a critical review. Carbon Capture Sci. Technol. 14, 100347.

Wenxing, Y., Weihai, L., Qingyuan, L., Xiaoru, L., Chao, C., 2025. Recent progress in CO_2 capture by porous solid materials. Ind. Eng. Chem. Res. 64, 4148–4178.

Zahir, M.H., Rahman, M.M., Irshad, K., Rahman, M.M., 2019. Shape-stabilized phase change materials for solar energy storage: MgO and $Mg(OH)_2$ mixed with polyethylene glycol. Nanomaterials 9 (1773). https://doi.org/10.3390/nano9121773, 1-21.

Zeng, L., Cheng, Z., Fan, J.A., Fan, L.S., Gong, J., 2018. Metal oxide redox chemistry for chemical looping processes. Nat. Rev. Chem. 2 (11), 349–364.

Zhang, K., Li, X.S., Duan, Y., King, D.L., Singh, P., Li, L., 2013. Roles of double salt formation and $NaNO_3$ in Na_2CO_3-promoted MgO absorbent for intermediate temperature CO_2 removal. Int. J Greenhouse Gas Cont. 12, 351–358.

Zhang, K., Li, X.S., Li, W.Z., Rohatgi, A., Duan, Y., Singh, P., Li, L., King, D.L., 2014. Phase transfer-catalyzed fast CO_2 absorption by MgO-based absorbents with high cycling capacity. Adv. Mater. Interfaces 1, 1400030.

Zhao, X., Ji, G., Liu, W., He, X., Anthony, E.J., Zhao, M., 2018. Mesoporous MgO promoted with $NaNO_3$/$NaNO_2$ for rapid and high-capacity CO_2 capture at moderate temperatures. Chem. Eng. J. 332, 216–226.

Zheng, Q., Huang, L., Zhang, Y., Wang, J., Zhao, C., Zhang, Q., Zheng, W., Cao, D., O'Hare, D., Wang, Q., 2016. Unexpected highly reversible topotactic CO_2 sorption/desorption capacity for potassium dititanate. J. Mater. Chem. A 4, 12889–12896.